New Formulation of Nonlinear Kinematic Hardening Model, Part I: A Dirac Delta Function Approach

Volodymyr Okorokov[*,,□], Yevgen Gorash[*], Donald Mackenzie[*] and Ralph van Rijswick[**]**

[*] University of Strathclyde, 99 George St, Glasgow, G1 1RD, the UK
[**]Weir Minerals, Venlo, 5928 PH

Abstract: A new mathematical modelling framework for simulation of metal cyclic plasticity is proposed and experimental validation based on tension-compression cyclic testing of S355J2 low carbon structural steel presented over the two parts of this paper. The advantages and limitations of the stress-strain curve shape modelling given by "Armstrong and Frederick" type hardening rules are discussed and a new formulation for kinematic hardening is proposed for more accurate representation of the stress-strain dependence under cyclic loading conditions. The proposed model is shown to describe the shape of the stress-strain curve accurately under various different loading conditions. Transition effects occurring at loading reversals are incorporated through a new framework of Dirac delta functions. In addition to the yield surface, stress supersurfaces able to expand and instantly move to simulate a shift of stress-strain curves during loading reversals are determined. This also enables inclusion of the behavior of monotonic stress-strain curves with yield plateau deformation in one mathematical model. The influence of the first stress invariant on the shape of a stress-strain curve in tension and compression directions observed in many metals is incorporated into the kinematic hardening rule. The ability of the model to accurately describe transition from elastic to elastic-plastic deformation at small offset strain yield points naturally accounts for nonlinearity of an unloading stress-strain curve after plastic pre-strain. Development of the model to include mixed cyclic hardening/softening, ratcheting and mean stress relaxation is presented in a companion paper (Part II), which includes experimental validation of the modelling framework.

Keywords: Cyclic plasticity, nonlinear kinematic hardening, low carbon steel, Dirac delta function

[□] volodymyr.okorokov@strath.ac.uk

1. Introduction

Elastic-plastic analysis of mechanical bodies is an important aspect of design and structural integrity assessment in a range of industries. The loading conditions considered in the analysis can vary significantly between applications, from relatively simple monotonic loading to complex load histories with multiple load and unload stages. The phenomenological approach to plasticity modelling which is based on macroscopic observations of material behavior and the concept of a yield surface in the stress space is a convenient way of structure behaviour prediction. The yield surface changes size and moves according to isotropic and kinematic hardening rules respectively, where, in simplest formulation, the plastic deformation is defined in terms of linear functions (Hill, 1950; Prager, 1949). These plasticity models are relatively simple to implement but are limited in their ability to represent real plastic behavior, particularly under cyclic loading conditions.

To describe cyclic plasticity more realistically, isotropic and kinematic hardening models are modified either through a multisurface approach (Dafalias and Popov, 1975; Mróz, 1967) or by introduction of nonlinear hardening functions. In the latter approach, a saturation function implemented through the Voce rule is used in isotropic hardening and a dynamic recovery term implemented through the Armstrong and Frederick (1966) rule (A-F rule) is used in kinematic hardening. These models are able to better represent experimentally observed plastic deformation under complex load cycles than the linear models. The A-F model was generalized by Chaboche (1979) by decomposing the back stress into several components. This model is widely used in practice, incorporated in several commercial Finite Element Method programs and is the basis of many other plasticity models incorporating various mathematical formulations for the dynamic recovery term. These types of model have been shown to give good agreement with experimental observation of ratcheting rate and stabilized stress-strain states for cyclic softening and hardening. However, Döring et al. (2003); Xu et al. (2016); Zhu et al. (2017) have shown that in many cyclic loading situations A-F models may not accurately capture the form of the evolving stress-strain curve, particularly during transitions at load reversals.

Several plasticity models that reasonably accurately represent the form of cyclic plasticity curves, including transition regions have been proposed. Döring et al. (2003) extended the Jiang and Sehitoglu (1996) model with A-F type of kinematic hardening to allow it to simulate transient behavior with reasonable accuracy for a wide strain range. The cyclic plasticity modelling framework of Zhu et al. (2014); Zhu et al. (2017); Zhu and Poh (2016) incorporates a new kinematic hardening rule in which the back stress is decomposed into long-range, middle-range and short range components with different nonlinear features. Each component consists of a special type of nonlinear kinematic hardening rule with a linear hardening term and a dynamic recovery term, resulting in a logarithmic function after integration for a monotonic loading step. The logarithmic function shows better prediction of the general stress-strain curve shape than the exponential function from the A-F rule, but still with certain deviations from experimental results. The authors attribute these to the fact that experimental results were fitted to only 3 components of back stress decomposition and the discrepancy is, in general, present in all Chaboche back stress decomposition models. The representation of the stress-strain curve can be improved by increasing the number of Chaboche back stress decompositions; however this can lead to highly complicated constitutive modelling and a complex procedure in the material specification process. To eliminate the issue of the numerous back stresses in Chaboche model frameworks, a phase mixture approach (Eisenträger et al., 2018a; Eisenträger et al., 2018b; Naumenko et al., 2011; Naumenko and Gariboldi, 2014) is applied for the unified description of the material behaviour to minimize the number of material parameters. The phase mixture model originates from materials science, i.e., hardening and softening behaviour is simulated based on an iso-strain composite with soft and hard constituents. It is assumed that the alloy is made of soft subgrains surrounded by hard boundaries, while the volume fraction of the hard constituent is closely related to the microstructure (e.g., mean subgrain size) and decreases toward a saturation value to model softening (Naumenko et al., 2011). To simplify parameter identification based on microstructural observations, a back stress and a softening variable are introduced as internal variables through a continuum mechanics approach (Naumenko et al., 2011; Naumenko and Gariboldi, 2014).

Many structural steels exhibit Lüders-type of yielding, in which a pronounce plateau occurs after yield such that plastic deformation takes place without increasing loading up to a point of subsequent strain hardening. This phenomenon has been studied experimentally for different materials, temperatures and loading conditions by Ballarin et al. (2009); Elliot et al. (2004); Wang and Huang (2017); Zhang and Jiang (2005b). The physical background of the phenomenon of the plateau together with advanced theoretical modelling by models of crystal plasticity and strain gradient plasticity are given by Hallai and Kyriakides (2013); Mazière et al. (2017); Yoshida et al. (2008). To solve a wide range of engineering problems, concerning structural plastic behaviour of different components, Goto et al. (1998); Shen et al. (1995); Ucak and Tsopelas (2011, 2012) included the yielding plateau into the phenomenological plasticity framework. Bounding surface and strain amplitude parameters dividing the loading into regions of plateau and strain hardening are introduced, allowing representation of loading and unloading from the plateau region with different hardening responses.

Nonlinear nature of unloading stress-strain curves after plastic pre-straining have been experimentally observed by Lee et al. (2017a); Lee et al. (2017b); Lee et al. (2013); Mendiguren et al. (2015); Yang et al. (2004); Yu (2009); Zajkani and Hajbarati (2017), who have reported reduction in measured unloading chord modulus of up to 40% of the initial value for different metals. This effect is usually neglected in modelling cyclic plasticity but is significant in engineering applications such as sheet metal forming, where spring-back due to elastic recovery occurs. Several mathematical models based on empirical relationships between Young's modulus and accumulated plastic pre-strain have been developed by (Chen et al., 2016); Luo and Ghosh (2003); Yoshida et al. (2002); Zang et al. (2006); Zavattieri et al. (2009). A review of the physical background of the phenomenon of nonlinearity of the unloading stress-strain curve slope is given by Chen et al. (2016). Explanation mechanisms, such as second order nonlinear elasticity via atomic bond stretching, twinning/detwinning, textural changes and material damage are excluded from consideration due to inconsistency with many sets of experimental results. The continuum elastic-plastic response due to internal and residual stresses and pile-up dislocation motion are established as two main mechanisms behind the phenomenon of elastic modulus reduction during accumulation of plastic strain.

Materials such as rocks and soils exhibit strong dependence of plastic flow on hydrostatic pressure. To incorporate this effect in a material model, all three stress invariants are usually considered in the constitutive equation (Lai et al., 2016; Shen et al., 2017; Smith et al., 2015; Sun et al., 2018). Some metals show a less pronounced dependence on hydrostatic pressure (Spitzig and Richmond, 1984) and the effect is introduced into yield criteria in several studies ((Wilson, 2001); (Brünig et al., 2000; Brünig et al., 2008; Brünig and Gerke, 2011; Cazacu and Barlat, 2004) (Bai and Wierzbicki, 2008; Mirone and Corallo, 2010). These indicate that stress triaxiality is important in predicting the onset of yield, as well as damage and fracture, in the metals considered. Hydrostatic pressure component is also present during the uniaxial tension-compression stress state. This effect on the form of cyclic stress-strain curves is observed in experimental curves from Halama et al. (2017); Kang et al. (2003); Kowalewski et al. (2014); Taleb and Cailletaud (2010); Voyiadjis et al. (2012); Wang et al. (2015) articles, where tension-compression plasticity tests showed a larger hardening effect for compression dominated loading. Voyiadjis et al. (2012) demonstrated that improved representation of this effect can be achieved by including the first stress invariant in the isotropic hardening constants.

The cyclic plasticity modelling concept proposed here accounts for the various plasticity phenomena identified above in a unified mathematical framework based on a nonlinear kinematic hardening rule with non-saturation effect and without back stress decomposition. The deformation process, including the transition effect between different stress-strain loops, is determined by a framework of Dirac delta functions and introduction of an additional stress surface. This approach can simulate stepwise dependence for different internal variables and is shown to be predictive in modelling transition of initial monotonic curves to subsequent cyclic plasticity curves. The effect of differences between tensile and compression stress-strain curves is represented by an incremental form of hardening slope dependency on the first stress invariant. The ability of the model to determine initiation of plasticity at the actual yield point means that unloading curve nonlinearity is included and the model naturally accounts for variation in Young's modulus during plastic strain accumulation without use of additional features to account for this phenomenon. The cyclic hardening/softening effects and ratcheting are considered in a companion paper (Part II). Experimental testing of S355J2 low carbon structural steel together with experimental results for other metals from the literature shows that the new model can accurately represent plasticity loop branches for different loading stages of loading.

2. Experimental setup

Tension-compression tests of S355J2 low carbon structural steel with chemical composition given in Table 1 were performed on a Zwick/Roell Amsler Z250 Material Testing Machine with capacity of 250 kN. The test specimen geometry and dimensions are shown in Fig. 1. Both strain and force control were used, with total strain rate of $5 \cdot 10^{-4}$ s^{-1} and stress rate of 1 MPa/s for both monotonic and cyclic loading. The strain was measured by a 10 mm gauge length extensometer. Preliminary tests were performed to determine the monotonic tensile behavior and material properties. Subsequent tests investigated different cyclic plasticity phenomena for specific loading programs under strain or force control as appropriate. Each specific loading program is described in the modeling sections of Part I and Part II of this study with reference to the specific phenomenon analysed.

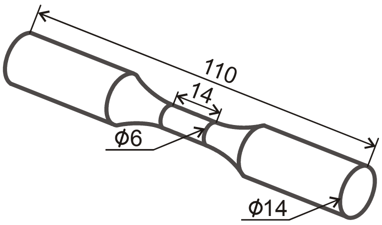

Fig. 1 – Geometry of tension-compression test specimen

The S355J2 material properties determined from monotonic tests are given in Table 2. It is noted that the measured monotonic yield stress of 255 MPa is lower than the nominal value for this type of steel, 355 MPa. The measured value conforms to the standard BSI (2000), which defines lower yield stress for S355 low carbon steel obtained after forging.

Table 1 - Chemical composition of S355J2 steel

Element	**C**	**Si**	**Mn**	**P**	**S**	**Cr**	**Ni**	**Mo**	**Al**	**B**
%	0.2	0.34	1.32	0.009	0.002	0.01	0.03	0.01	0.042	0.0012

Table 2 – Basic mechanical properties of S355J2 steel

Yield strength	**Tensile strength**	**Elongation**	**Young's modulus**
255 MPa	501 MPa	34.5 %	200 GPa

3. Modelling background

The proposed nonlinear kinematic hardening model is based on observations made during the experimental investigation of S355J2 low carbon steel. It will be shown that the general form of the rule is valid for other metals, with particular forms of the evolution variables required for different materials.

The model is based on the small strain assumption with strain decomposition on elastic and plastic parts:

$$\varepsilon_{ij} = \varepsilon_{ij}^{e} + \varepsilon_{ij}^{p} \tag{1}$$

The elastic part of the strain tensor is described with the Hooke's law for isotopically elastic materials in the form:

$$\sigma_{ij} = E_{ijkl}\varepsilon_{kl}^{e} \tag{2}$$

where σ_{ij} is Cauchy stress tensor and E_{ijkl} is elastic stiffness tensor defined as:

$$E_{ijkl} = \lambda\delta_{ij}\delta_{kl} + G\left(\delta_{ik}\delta_{jl} + \delta_{il}\delta_{jk}\right) \tag{3}$$

Parameters λ and G are defined as:

$$\lambda = \frac{\nu E}{(1+\nu)(1-2\nu)} \qquad G = \frac{E}{2(1+\nu)} \tag{4}$$

where E is Young' modulus and ν is Poisson's ratio.

This study considers mathematical modelling of rate independent cyclic plasticity for metals. The classical concept of the yield surface in the form of von Mises criterion within the framework of rate-independent plasticity is adopted:

$$f = \sqrt{\frac{3}{2}\left(S_{ij} - X_{ij}\right)\left(S_{ij} - X_{ij}\right)} - R - \sigma_0 \tag{5}$$

where σ_0 is initial yield stress, S_{ij} is deviatoric part of the stress tensor, R is isotropic hardening function and X_{ij} is back stress tensor responsible for kinematic hardening.

With the assumption of plastic incompressibility observed for most of metals, the plasticity flow is described with the use of the flow rule associated with the yield surface in the following form:

$$\dot{\varepsilon}_{ij}^{p} = \frac{3}{2}\frac{S_{ij} - X_{ij}}{R + \sigma_0}\dot{p} \tag{6}$$

Appropriate forms of isotropic hardening R and kinematic hardening X_{ij} for accurate modelling of a variety of cyclic plasticity phenomena are identified from the results of the S355J2 steel test programme.

4. Determination of cyclic yield strength and isotropic hardening rule

To determine the evolution rule for expansion of the yield surface (5) and a mathematical form for the isotropic hardening variable, the cyclic yield strength of the material was determined. A crucial factor in the yield strength determination is accurate measurement of the yield point. Abdel-Karim (2011) discussed various methods of yield stress determination, which significantly affect the choice of the yield surface and hardening rules. The S355J2 steel exhibits discontinuous yield under monotonic test but a notable deviation from linearity was observed at stress levels below the upper yield point. This behavior is common in polycrystalline metals, where local plasticity can occur at relatively low stress levels due to beneficial orientation of crystals. In design practice, the yield point of a continuous yielding material is defined as the stress corresponding to 0.2% plastic strain. A similar approach is adopted here but for more accurate representation of the plasticity phenomena the yield point is defined at 0.01% offset plastic strain. This gives a yield stress value of 90 MPa, which is significantly lower than the upper yield stress of 255MPa at which macroscopic yield occurs and the Lüders plateau initiates, as shown in Fig. 2. The deformation between the defined yield point and the upper yield stress is not non-linear elasticity, but rather can be explained as inhomogeneous localized plastic strain of favourably oriented single grains as discussed by Jiang (2001); Zhang and Jiang (2005a). Determination of the initial yield stress and the hardening law for plastic deformation between the initial and plateau upper yield stresses is important as it accounts for the phenomenon of cyclic softening at a small plastic strain range, as discussed in the companion paper (Part II).

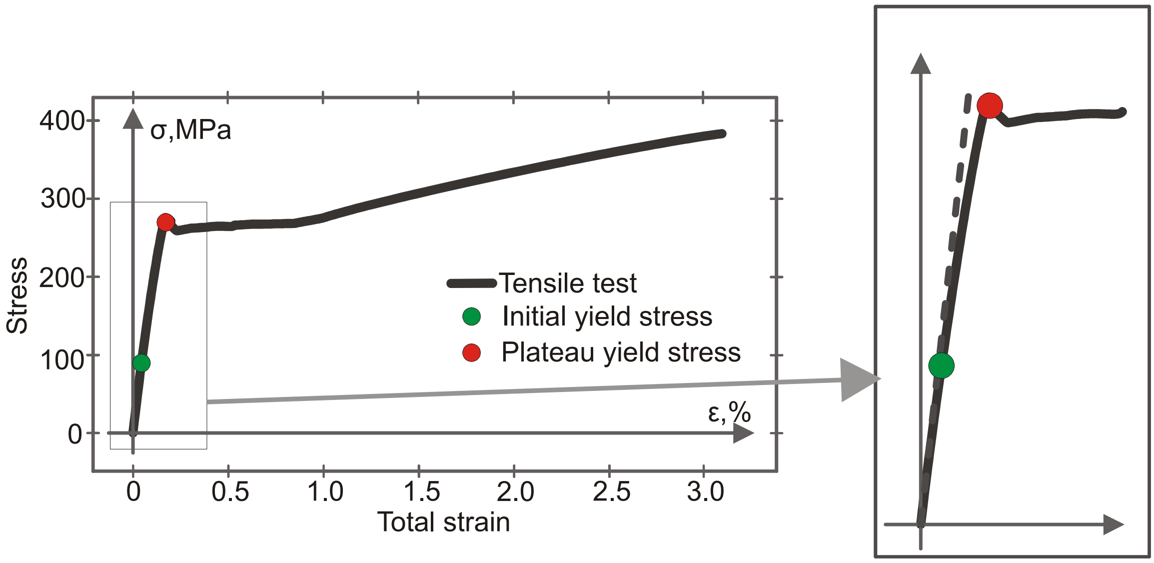

Fig. 2 – Determination of the two yield stresses for S355J2 steel

To define the yield strength under cyclic loading conditions, values of yield stress were determined for stress-strain curves from loading-unloading stages, random loading sequences and stabilized hysteresis loops, as shown in Figs 3a, 3b and 3c respectively. Figure 3d shows the measured yield stress values in terms of stress within the elastic domain plotted against the plastic strain accumulated prior to yield stress measurement. It is seen that the elastic domain gradually decreases within the range 0.1% to 1.0% of accumulated plastic strain and then remains unchanged within a 20 MPa scatter band. This suggests that the radius of the yield surface is reduced after initial plastic strain accumulation and then remains constant with plastic strain accumulation regardless of plastic deformation history. This material behavior can be modelled by the use of a nonlinear isotropic hardening rule adopted in many plasticity models:

$$\dot{R} = b\left(Q - R\right)\dot{p} \tag{7}$$

where b and Q are material constants. The saturation nature of the dependence shown in Fig. 3d indicates the nonlinear isotropic hardening rule (7) is an appropriate choice for isotropic hardening modeling.

5. Stress-strain curve shape modelling

Experimental measurement of the yield stress during different loading conditions determined the shape of the yield surface and the isotropic hardening rule for its change in size. The size of the elastic domain remains unchanged during plastic deformation for the investigated S355J2 steel. Subsequently, the stress-strain curve shape and variation between curves during the deformation process are uniquely described by the kinematic hardening rule, which defines translation of the yield surface.

The A-F type of kinematic hardening law for yield surface translation is widely used in the literature:

$$\dot{X}_{ij} = \frac{2}{3}\bar{C}\dot{\varepsilon}_{ij}^{p} - \bar{\gamma}X_{ij}\dot{p} \tag{8}$$

where $\bar{C}$ and $\bar{\gamma}$ are material constants and $\dot{p}$ is accumulated plastic strain rate defined as:

$$\dot{p} = \sqrt{\frac{2}{3}\dot{\varepsilon}_{ij}^{p}\dot{\varepsilon}_{ij}^{p}} \tag{9}$$

Integration of (8) for a tensile loading step gives an exponential function in the form:

$$X = \frac{\bar{C}}{\bar{\gamma}}\left(1-\exp\left(-\bar{\gamma}\varepsilon^{p}\right)\right) \tag{10}$$

where X is uniaxial back stress and ε^{p} is uniaxial plastic strain.

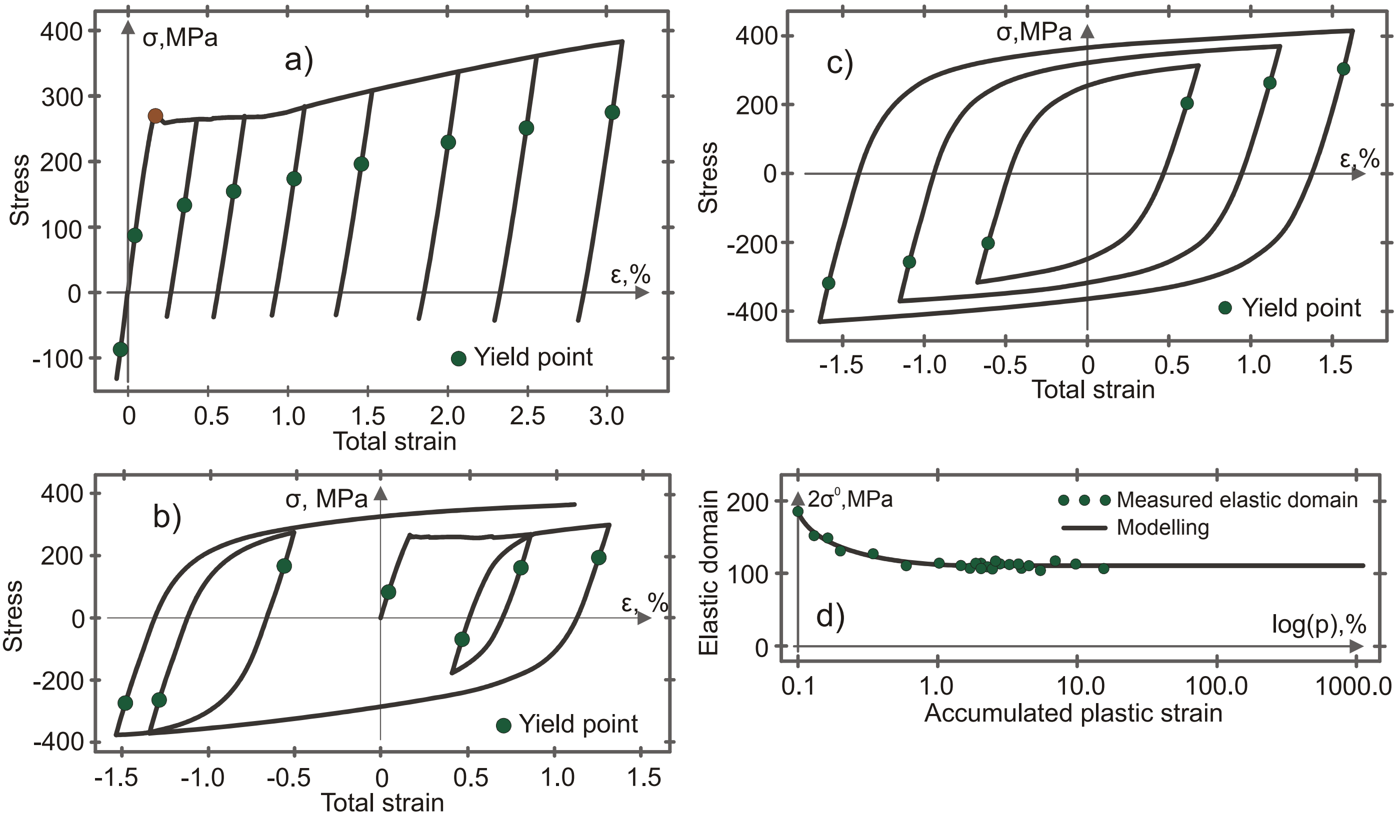

Fig. 3 – Measurement of cyclic yield strength of S355J2 steel in cases of (a) loading-unloading curves, (b) stabilized hysteresis loops and (c) stress-strain curves from random loading; (d) measured elastic domain vs. accumulated plastic strain

This type of function has a saturation effect. However, most metals, and specifically the S355J2 steel considered here, does not show saturation of stresses during plastic deformation in the investigated range. Therefore, to describe the stress-strain curve shape more precisely, Chaboche back stress decomposition is applied, where back stress is presented as a sum of several components:

$$\dot{X}_{ij}^{(k)} = \bar{C}^{(k)}\dot{\varepsilon}_{ij}^{p} - \bar{\gamma}^{(k)}X_{ij}^{(k)}\dot{p} \tag{11}$$

$$X_{ij} = \sum_{k=1}^{n} X_{ij}^{(k)} \tag{12}$$

where n is number of back stress decompositions.

The kinematic hardening rule (8) with decomposition (11) has shown reasonable prediction ability for many cyclic plasticity phenomena. However, significant variation of plastic modulus in experimental responses of cyclic hardening and softening during cyclic loading, as well as the difference between the initial monotonic and subsequent cyclic curves, requires additional modification of this model. More accurate description of the transition between stress-strain curves at load reversals and modelling deformation history with ratcheting and hardening/softening effects is achieved by complex modifications proposed by Döring et al. (2003); Jiang and Sehitoglu (1996). According to the proposed models, higher accuracy of the simulation responses is achieved by the use of several back stress decompositions, usually $n \geq 6$. A large number of back stress decompositions are inherently related to the exponential function, as a result of integration of (8). To reduce the number of back stress decompositions, Zhu et al. (2017); Zhu and Poh (2016) have proposed a new kinematic hardening law, where a long range back stress is expressed as:

$$\dot{X}_{ij} = \frac{2}{3}\hbar\dot{\varepsilon}_{ij}^{p} - \frac{\zeta^{m+2} q X_{eq}^{m}}{\hbar^{m}\left(1+\zeta q\right)\ln\left(1+\zeta q\right)^{(m+1)}} X_{ij}\dot{p} \tag{13}$$

This type of kinematic hardening law has a logarithmical form after integration for a monotonic loading step:

$$X = \frac{\hbar}{\xi} B \ln\left(\xi\varepsilon^{p} + 1\right) \tag{14}$$

Application of the Zhu et al. (2017) model has shown better description of the monotonic and cyclic stress-strain curves than exponential A-F models, with the use of only 3 back stress decompositions. The accuracy of the model is achieved due to the form of the logarithmic function (14), which naturally fits the nonlinear slope of metal elastic-plastic deformation.

It is noted that the kinematic hardening law (13) gives the logarithmic function (14) only under integration with zero initial conditions $X\left(0\right) = 0$. Consequently, analytical calibration of the model to the case of a branch of the hysteresis loop with non-zero initial conditions is difficult. To provide an analytical solution for integration of the kinematic hardening law, applying to any loading step of uniaxial proportional loading, and to further improve the simulation accuracy for the stress-strain curve shape, a new kinematic hardening rule is proposed here:

$$\dot{X}_{ij} = AB\exp\left(-\frac{4}{9}\frac{X_{eq}\overline{r}_{kl}n_{kl}}{B}\right)\dot{\varepsilon}_{ij}^{p} \tag{15}$$

where A and B are material parameters and n_{ij} is a unit direction of plastic flow:

$$n_{ij} = \frac{\partial f}{\partial \sigma_{ij}} = \frac{3}{2}\frac{S_{ij} - X_{ij}}{\sigma_{eq}} \tag{16}$$

Equivalent back stress X_{eq} is defined as:

$$X_{eq} = \sqrt{\frac{3}{2} X_{ij} X_{ij}} \tag{17}$$

and $\overline{r}_{kl}$ is a unit direction of the radius vector of back stress tensor:

$$\vec{r}_{ij} = \frac{3}{2}\frac{X_{ij}}{X_{eq}} \tag{18}$$

It is noted that the proposed kinematic hardening rule in the form of (15) does not contain the dynamic recovery term, which provides directionality of hardening under non-proportional loading in A-F rules. Directionality of the kinematic hardening rule (15) is provided by the term $\overline{r}_{kl}n_{kl}$, as demonstrated in Fig. 4. The inner product of the yield surface normal and back stress radius vector provides different hardening depending on the direction of loading. In the case of proportional loading, the normal and radius vector can either coincide or be opposite in direction, giving values of the inner product equal to 1.5 or -1.5 respectively.

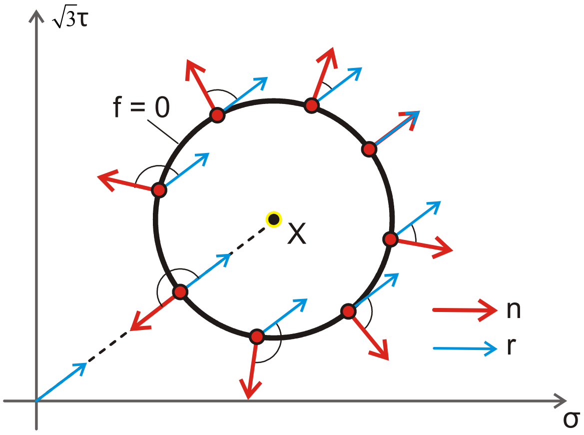

Fig. 4 – Representation of the directional behaviour of the proposed kinematic hardening rule (15)

Using (17) and (18), equation (15) can be rewritten in the following form:

$$\dot{X}_{ij} = AB\exp\left(-\frac{2}{3}\frac{X_{kl}n_{kl}}{B}\right)\dot{\varepsilon}_{ij}^{p} \tag{19}$$

Integration of the kinematic hardening rule (19) for the case of uniaxial tensile load gives the logarithmic function:

$$X = \frac{3}{2}B\ln\left(A\varepsilon^{p}+1\right) \tag{20}$$

Figure 5 shows that application of the new kinematic hardening rule to the stress-strain curve shape of a single hysteresis loop branch provides accurate modelling with the use of only two material parameters and no back stress decomposition.

6. Shift of the stress-strain curves

Although the proposed kinematic hardening rule describes the shape of a single deformation stress-strain curve precisely, its direct application to all deformation curves at the same time will deviate from experimental results. This is due to the shift of stress-strain curves that occurs with reversal of load path. To determine the effect load reversals on the plastic deformation history, it is convenient to investigate the measured stress-strain curves for S355J2 steel from a random loading program as shown in Fig. 6a. Figure 6b represents the deformation curves in terms of back stress vs. plastic strain. It can be noticed that all stress-strain curves share similar shape, if they compared relatively a certain reference point *O*. To demonstrate this, all the deformation curves are plotted on the same graph with the reference point *O* in the beginning of the coordinate system in Fig. 6c. All curves are precisely described by the use of the logarithmic function (20), however with different values of *A* and *B* parameters. This difference is contributed to cyclic hardening/softening and asymmetry between tension and compression and will be addressed in the following sections and in the companion paper (Part 2).

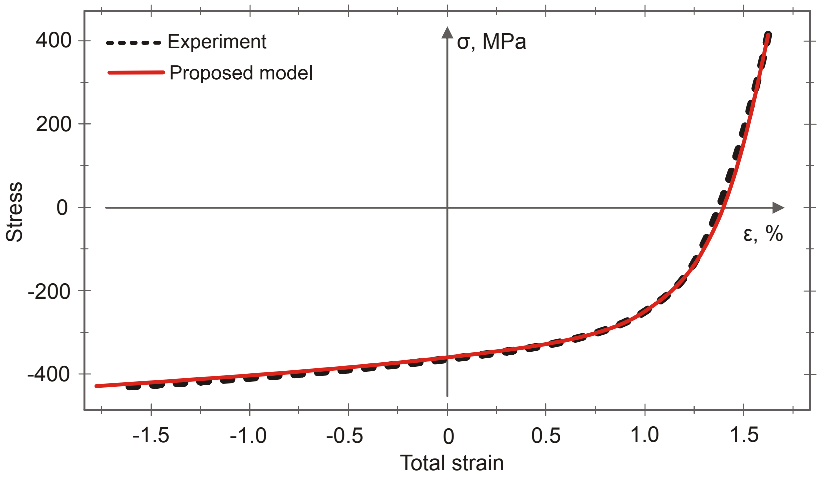

Fig. 5 – Modelling of stress-strain curve shape for a branch of stabilized hysteresis loop of S355J2 steel

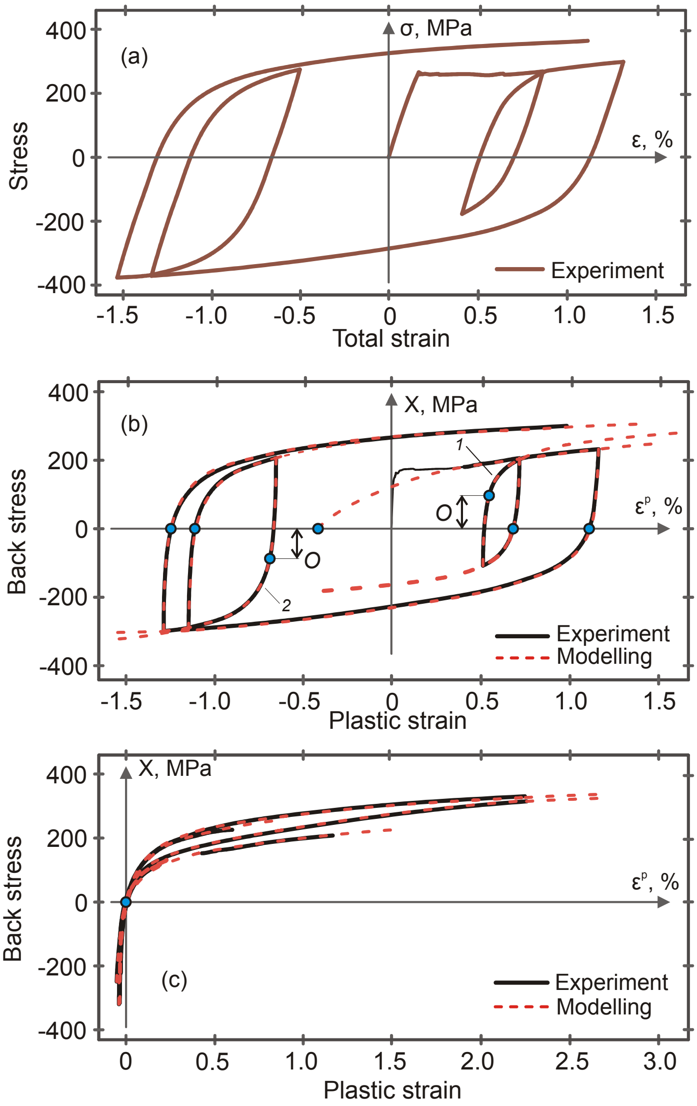

Fig. 6 – Stress-strain response under random loading for S355J2 steel in terms of (a) stress vs. total strain, (b) back stress vs plastic strain and (c) back stress vs. plastic strain with reference point at the beginning of the coordinate system

It can be assumed that the stress-strain curves from the deformation process are accurately described by the proposed kinematic hardening law (19), where the curves occur with a specific value of shift of reference point *O*. A modification has to be made to include this shift into the kinematic hardening rule. Equation (19) can be written for a tension-compression load cycle as:

$$\dot{X} = \frac{3}{2} AB \exp\left(s \frac{2X}{3B} \right) \dot{\varepsilon}^p \qquad \begin{cases} s = -1 & \text{for tension} \\ s = 1 & \text{for compression} \end{cases} \tag{21}$$

Integration of (21) with $X\left(\varepsilon_0^p\right) = X_0$ gives:

$$X = \frac{3}{2} sB \ln\left[sA\left(\varepsilon^p - \varepsilon_0^p\right) + \exp\left(-s \frac{2X_0}{3B} \right) \right] \tag{22}$$

To include the shift of reference point *O*, the kinematic hardening rule is modified to the form:

$$\dot{X} = \frac{3}{2} AB \exp\left(s \frac{2(X - O)}{3B} \right) \dot{\varepsilon}^p \tag{23}$$

Integration of (23) with $X\left(\varepsilon_0^p\right) = X_0$ gives an equation describing the deformation process for tension-compression loading accounting for the shift of the stress-strain curves:

$$X = \frac{3}{2} sB \ln\left[sA\left(\varepsilon^p - \varepsilon_0^p\right) + \exp\left(-s \frac{2(X_0 - O)}{3B} \right) \right] + O \tag{24}$$

Fig. 6b shows that equation (24) precisely describes the stress-strain curve at load reversals. Equation (23) is generalised to the multiaxial case in the form of:

$$\dot{X}_{ij} = AB \exp\left(-\frac{2}{3} \frac{\left[X_{kl} - O_{kl}\right] n_{kl}}{B} \right) \dot{\varepsilon}_{ij}^p \tag{25}$$

where O_{kl} is back stress reference tensor.

The general form of equation (25) is valid for modelling the stress-strain curve shape for many materials. Figure 7 shows examples of application to hysteresis loops for 304 and X10CrMoVNb9-1 steels, 2124-T851 aluminum alloy and pure copper. It is seen that the new kinematic hardening model has good prediction accuracy for the stress-strain curve shapes for these materials. To simulate other plasticity phenomena such as the transition behaviour between cyclic curves and modelling of the initial monotonic stress-strain curve, the expression for back stress reference tensor O_{ij} should be developed specifically for different materials.

The next requirement is to develop an evolution rule for the shift of back stress reference tensor O_{ij} with application to the investigated S355J2 steel. To evaluate the behaviour of reference point *O* based on uniaxial tension-compression testing, experimental results for stress-strain response from Fig. 8a are analysed. Fig. 8b shows this stress-strain response in terms of back stress versus plastic strain, where reference points from each curve are numbered from 1 to 8. It can be assumed that the reference point stays unchanged during active loading step and changes its value only on load reversal, such as from Curve 2 to Curve 3, or with return of load to the main curve, such as from Curve 3 to Curve 1. Evolution of the reference point *O* with accumulation of plastic strain can therefore be plotted as a stepwise dependence, as shown in Fig. 8c. This type of dependence requires consideration of a new mathematical approach to model this type of behaviour.

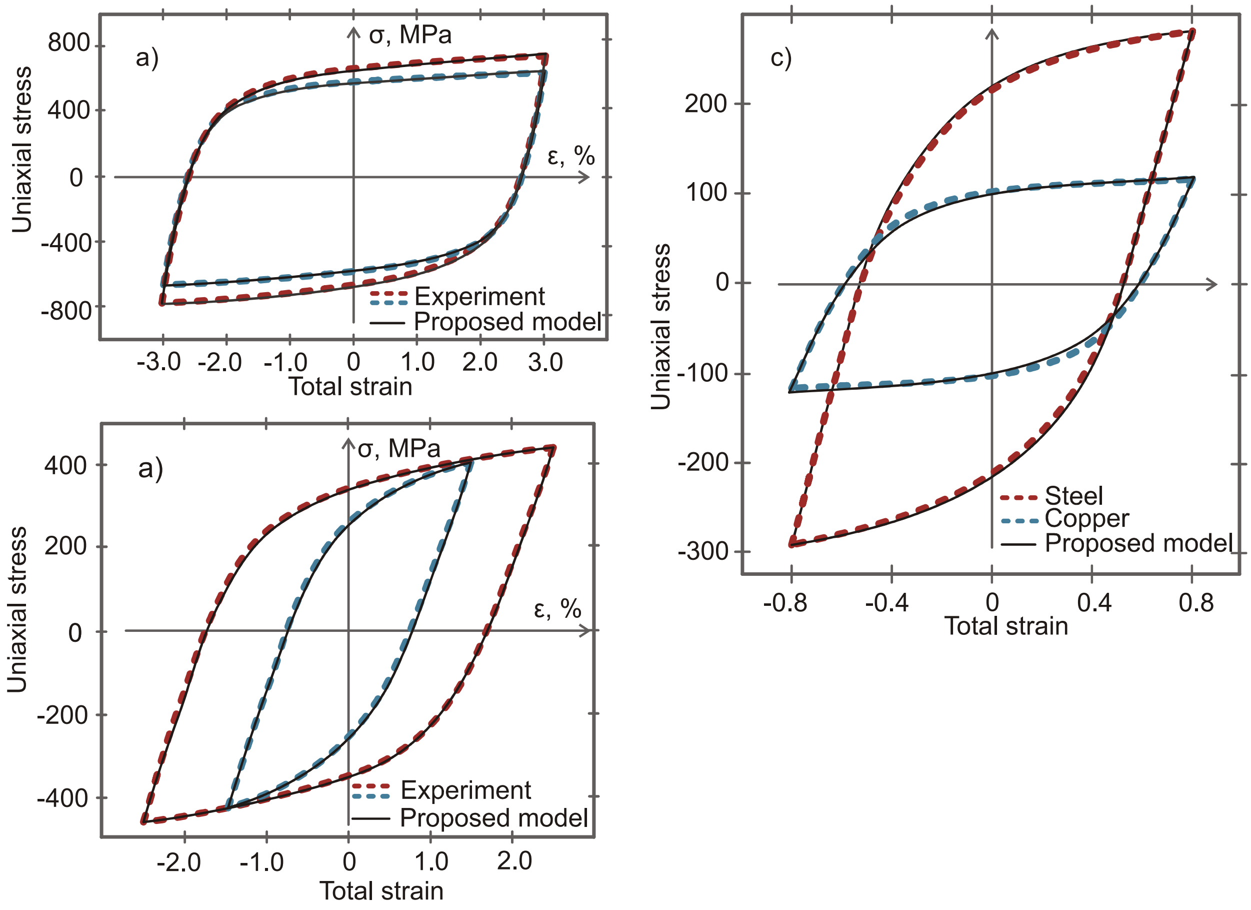

Fig. 7 – Stress-strain curves from hysteresis loops branches for (a) 304 stainless steel (Kang et al., 2003), (b) 2124-T851 aluminum alloy (Halama et al., 2017) and (c) X10CrMoVNb9-1steel and pure copper (Kowalewski et al., 2014)

7. Dirac delta functions framework

Developing a new mathematical framework for describing cyclic plasticity phenomena is required for a certain types of internal variables which behave as constants during certain intervals of loading. An example of such a variable is previously accumulated plastic strain, introduced by Voyiadjis et al. (2012) to better describe stress-strain curve prediction. The concept of this variable is that previously accumulated plastic strain remains constant during a step of active loading and changes to the current value of accumulated plastic strain only with a change of loading from tensile to compressive or vice versa. In this study, this type of variables is widely and efficiently used for various different cases and strict mathematical representation is first given here based on a framework of Dirac delta functions.

When an internal variable is kept constant during some time interval, the history of its development is described by a stepwise function as shown in Fig. 9. To reproduce this type of dependency in evolution laws, a Dirac delta function $\delta(x)$ is used here. The Dirac delta function is formulated as:

$$\delta(x) = \begin{cases} +\infty, & x = 0 \\ 0, & x \neq 0 \end{cases} \tag{26}$$

The evolution equation for internal variables with stepwise dependency is written by means of the Dirac delta function (26) in a general form:

$$\dot{\chi} = \delta\left[g(x,\chi)\right] f(x,\chi)\,\dot{x} \tag{27}$$

Several basis properties of the Dirac delta functions are used to solve the general equation (27). The main property is that integration of a differential equation $\dot{\chi}(x)=\delta(x)\dot{x}$ with initial condition of $\chi(0)=0.5$ yields $\chi(x)=H(x)$. $H(x)$ is the Heaviside step function, defined as:

$$H(x)=\begin{cases}1, & x=0\\ 0, & x<0\end{cases} \tag{28}$$

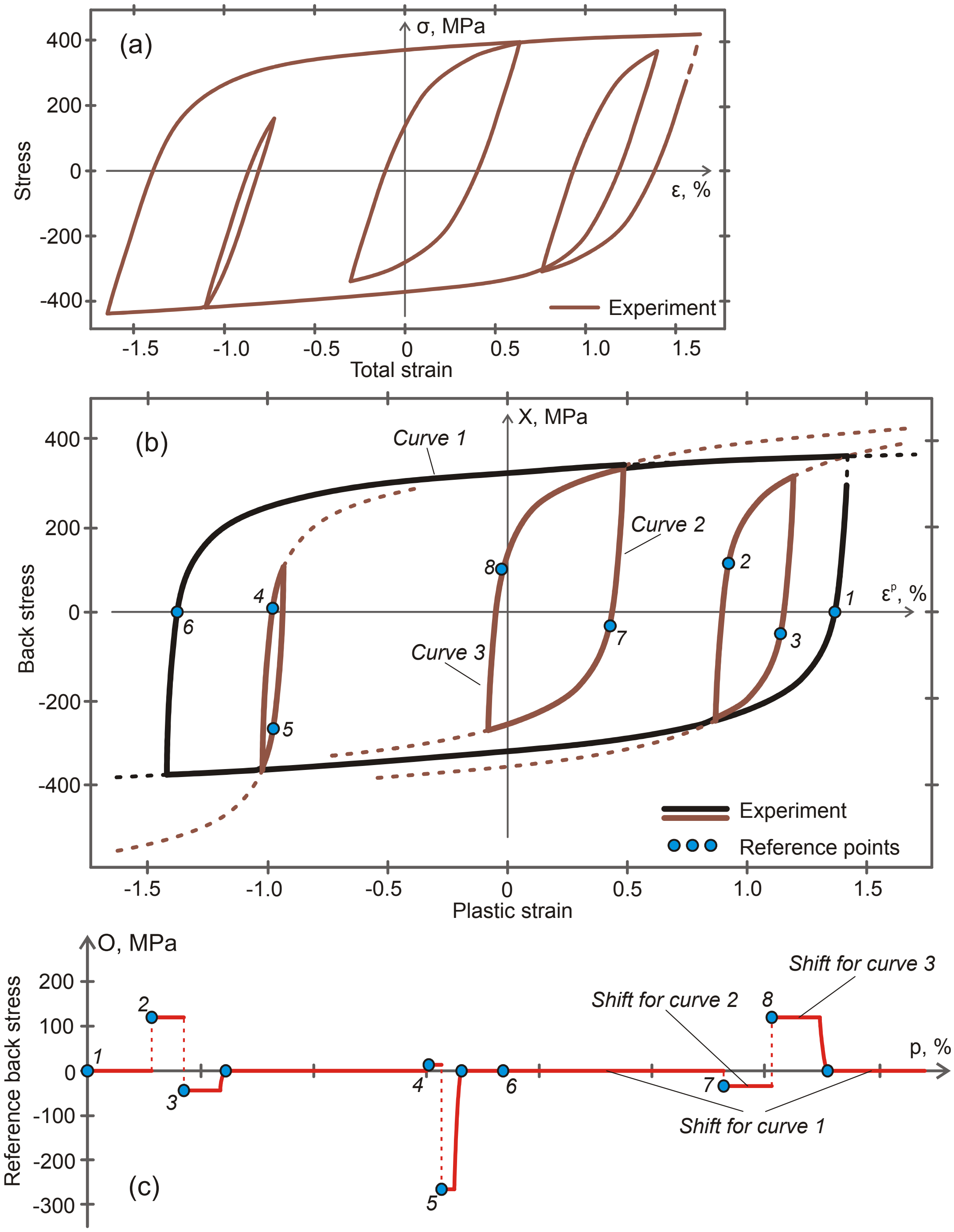

Fig. 8 – Stress-strain response under random loading for S355J2 steel in terms of (a) stress vs. total strain, (b) back stress vs plastic strain; (c) behavior of the reference point with accumulation of plastic strain

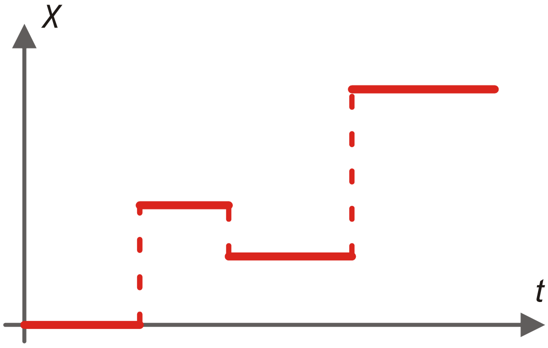

Fig. 9 – Stepwise dependence of internal variable

Additional properties of the Dirac delta function are summarized in Table 3. For the sake of numerical performance it is convenient to write the Dirac delta function in the approximate form:

$$\delta(x) = \lim_{a \to 0} \phi(x, a) \tag{29}$$

The function $\phi(x,a)$ which is associated with the Dirac delta function can be taken as:

$$\phi(x,a) = \frac{\exp(-\frac{x^2}{a^2})}{a\sqrt{\pi}} \tag{30}$$

It is important that representation of the Dirac delta function in the form of (30) keeps its properties for solving of differential equations.

An instant change of an internal variable, such as the shift of the reference point in a stress-strain curve shown in Fig. 8c, can be modelled by tuning the parameter a in the delta function $\phi(x,a)$ to be small. Adjusting this parameter to larger values can provide more gradual transition for internal variable changes, such as transition between Curve 3 to Curve 1 of Fig. 8b. The definition of the a parameter is important as it is a unique parameter for evaluation of ratcheting and mean stress relaxation.

Table 3 – Properties of Dirac delta function for solving of differential equations

Equation	Solution
$\dot{\chi}(x) = \delta(x-k)\dot{x}$ (3.1)	$\chi(x) = H(x-k) + c_1$ (3.7)
$\dot{\chi}(x) = c\delta(x-k)\dot{x}$ (3.2)	$\chi(x) = cH(x-k) + c_1$ (3.8)
$\dot{\chi}(x) = \delta[x - g(y)]\dot{x}$ (3.3)	$\chi(x) = H[x - g(y)] + c_1$ (3.9)
$\dot{\chi}(x) = g(x)\delta(x-k)\dot{x}$ (3.4)	$\chi(x) = g(k)H(x-k) + c_1$ (3.10)
$\dot{\chi}(x) = [\delta(x) + g(x)]\dot{x}$ (3.5)	$\chi(x) = H(x) + \int_0^x g(y)\,dy + c_1$ (3.11)
$\dot{\chi}(y) = \delta(y)\dot{y},\ y = x(\xi)$ $\dot{\chi}(\xi) = \delta[x(\xi)]\frac{\dot{y}}{\dot{\xi}}\dot{\xi}$ (3.6)	$\chi(\xi) = H(x(\xi)) + c_1$ (3.12)

8. Developing of the evolution equation for shift of back stress reference tensor

Investigation of the deformation curve from Fig. 8 suggests that there are two main reasons for changing the reference point of the stress-strain curves. The first case is change of the loading direction such as from Curve 2 to Curve 3 and the second case is transition between two curves without changing loading path such as from Curve 3 to Curve 1. It is assumed that the shift point keeps constant during a step of loading and changes its value only when Case 1 or Case 2 occurs.

8.1 Case 1

The shift point of the deformation curves changes its value whenever loading path changes to completely reversal such as from tensile to compression loads. To understand the movement of the shift point a specific test with several cycles of tension-compression with loading program shown in Fig. 10a are considered. Figure 10b demonstrates the results of the test in terms of stress-strain response. To analyse the stress-strain response, deformation curves are plotted in coordinates of uniaxial back stress vs. uniaxial plastic strain and shown in Fig. 10c. It can be noticed from the graph that the shift point changes its value from zero to a non-zero value with every reversal of loading when loading cycles are confined within a range of compressive and tensile stresses where maximum amplitude is attained in tension as shown by Curve 1. As soon as the peak stress of a hysteresis loop such as from Curve 2 or 3 exceeds this stress range in either tensile or compression direction, no further shift of the reference point occurs anymore regardless of new reversals of loading cycles. This observation suggests the existence of a stress surface within which the reference point of the deformation curve can shift. Once the current stress state is on the surface the reference point returns to the zero value. As the back stress surface is located outside the yield surface it is called a supersurface and introduced as:

$$F_0^s = X_{eq} - R_s \tag{31}$$

where R_s is the radius of the supersurface.

The supersurface can isotopically change in size without kinematic movement of its centre. The evolution law of R_s based on consistency condition is formulated as:

$$\dot{R}_s = H\left(F_0^s\right)\frac{\dot{X}_{eq}}{\dot{p}}\dot{p} \tag{32}$$

$\dot{X}_{eq}/\dot{p}$ is calculated as:

$$\frac{\dot{X}^{eq}}{\dot{p}} = \frac{\partial X_{eq}}{\partial p} + \frac{\partial X_{eq}}{\partial X_{ij}}\frac{\dot{X}_{ij}}{\dot{p}} = \frac{2}{3}\frac{X_{ij}}{X_{eq}}AB\exp\left(-\frac{2}{3}\frac{\left[X_{kl}-O_{kl}\right]n_{kl}}{B}\right)n_{ij} \tag{33}$$

The Heaviside function $H\left(F_0^s\right)$ means that the variable R_s can only evolve when the current stress state is on the supersurface F_0^s and stays unchanged while the stress state is inside the supersurface.

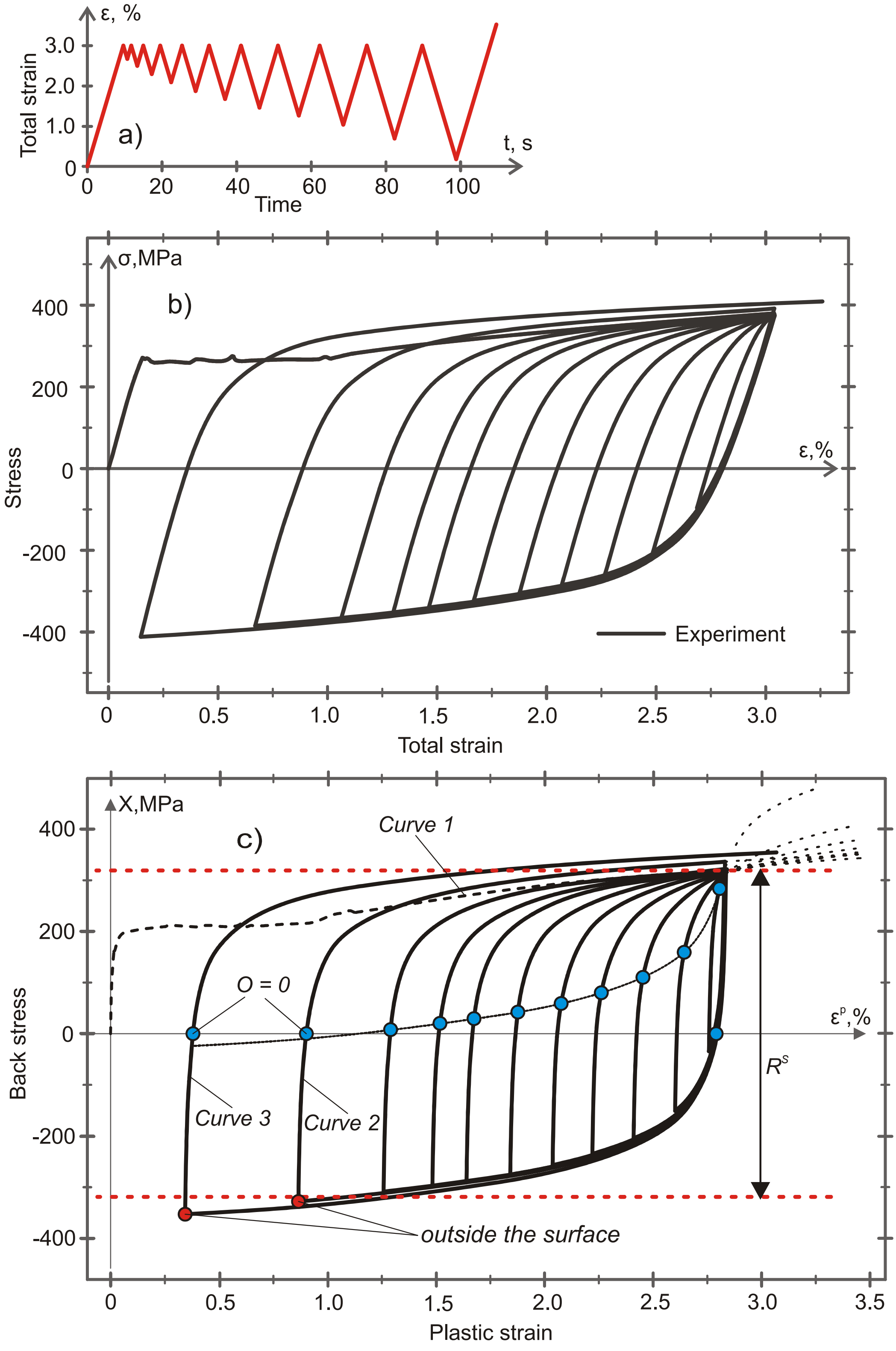

Fig. 10 – Testing with loading to define supersurface; (a) loading program , (b) stress vs. total strain and (c) back stress vs plastic strain

To develop the evolution rule for the shift of back stress reference tensor for Case 1, loading, unloading and reloading steps for uniaxial case are considered in Fig. 11. Its generalization for the multiaxial case is presented in Fig. 12. Starting from initial point A, the load path to point B evolves the reference supersurface. Reversal of the load path occurs at point B. At that moment, the current stress state goes inside the supersurface satisfying the condition $F_0^s < 0$. With reversal of the load path, deformation proceeds from point B to point C. To establish the evolution rules for the back stress reference tensor O_{ij}, the uniaxial case of unloading from Fig. 11a is generalised as follows. Reversal of the loading path at point B creates subsurface f^s which is associated with reference supersurface F_0^s. These have a mutual point which is defined as the back stress attained at a moment of load reversal. The location of the back stress reference point on the subsurface depends on the current stress state. The back stress reference point is defined as a half of the distance between the point of previously attained back stress and the point of intersection between a supersurface and the normal of the yield surface. This definition allows the back stress reference point to always lie on the subsurface f^s. It also accounts for anisotropy of hardening during non-proportional loading conditions. The equation for the back stress reference tensor is then written as:

$$O_{ij} = \frac{1}{2}\left(Z_{ij} - \overline{X}_{ij}\right) \tag{34}$$

where Z_{ij} is the tensor of intersection between the supersurface and the normal to the yield surface and $\overline{X}_{ij}$ is the previously attained back stress tensor.

The intersection between the supersurface and the normal to the yield surface is determined using geometrical properties of the intersection between a line and a hypersphere in a multidimensional space. The line and sphere equations are written in the form:

$$\text{Line: } x_{ij} = X_{ij} + n_{ij}\beta \tag{35}$$

$$\text{Hypersphere: } \left(x_{ij} - \overline{c}_{ij}\right)\left(x_{ij} - \overline{c}_{ij}\right) = \frac{2}{3}R_s^{\,2} \tag{36}$$

where $\overline{c}_{ij}$ is a centre of the supersurface and β is a parameter for parametrical representation of the line.

Parameter β can be found with roots of quadratic equation $\mu_1\beta^2 + \mu_2\beta + \mu_3 = 0$ as:

$$\beta = \frac{-\mu_2 \pm \sqrt{\mu_2^{\,2} - 4\mu_1\mu_3}}{2\mu_1} \tag{37}$$

where coefficients of the quadratic equation μ_1, μ_2 and μ_3 are determined as:

$$\begin{aligned} \mu_1 &= n_{ij}n_{ij} = 1.5 \\ \mu_2 &= 2n_{ij}\left(X_{ij} - \overline{c}_{ij}\right) \\ \mu_3 &= \left(X_{ij} - \overline{c}_{ij}\right)\left(X_{ij} - \overline{c}_{ij}\right) - \frac{2}{3}R_s^{\,2} \end{aligned} \tag{38}$$

As the quadratic equation has two roots, it corresponds to two points of intersection. The point in the positive direction of the yield surface normal should be chosen for the solution.

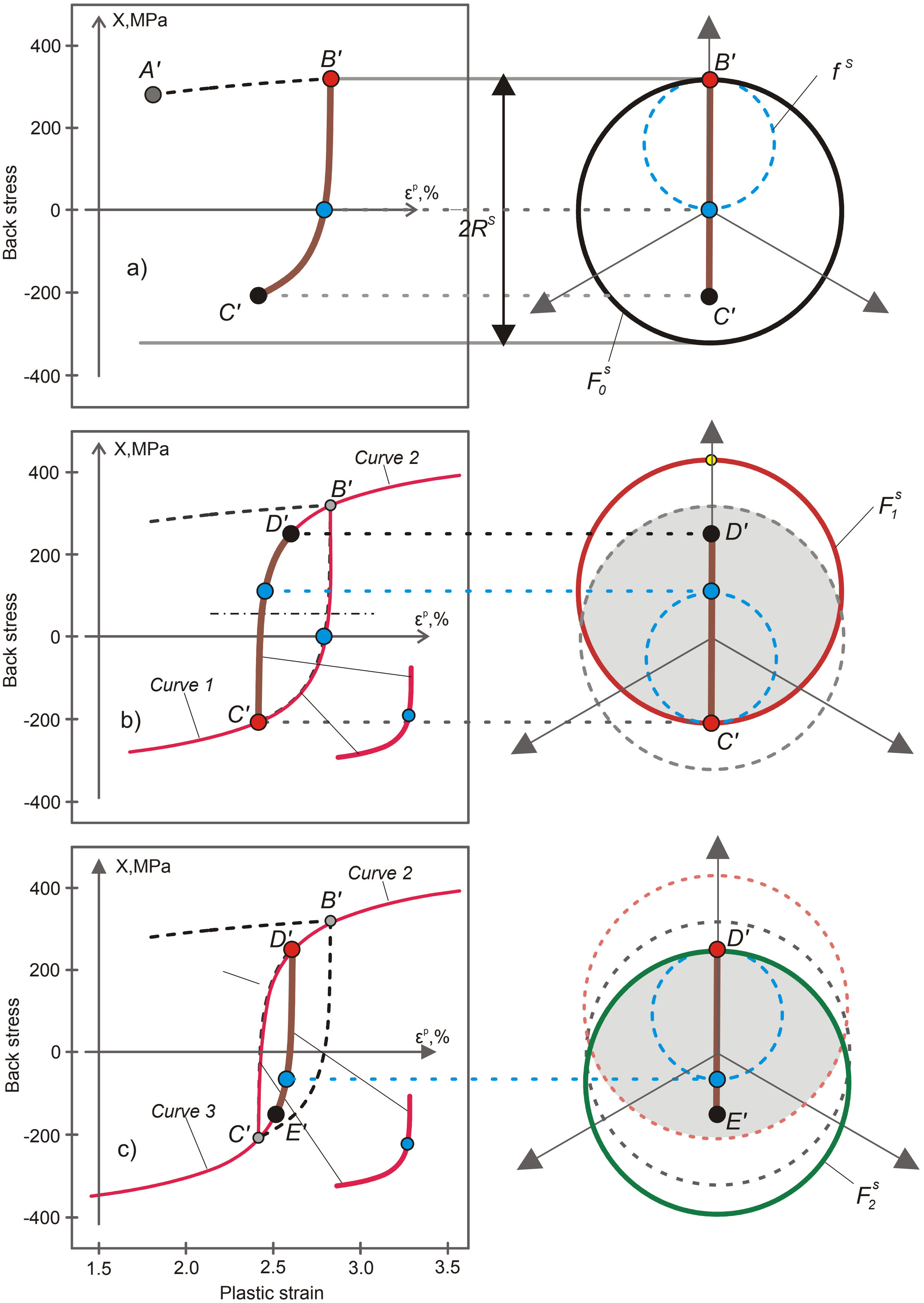

Fig. 11 – Consideration of three paths of tension-compression tests with multiaxial representation; (a) loading from A' to C' , (b) loading from C' to D' and (c) loading from D' to E'

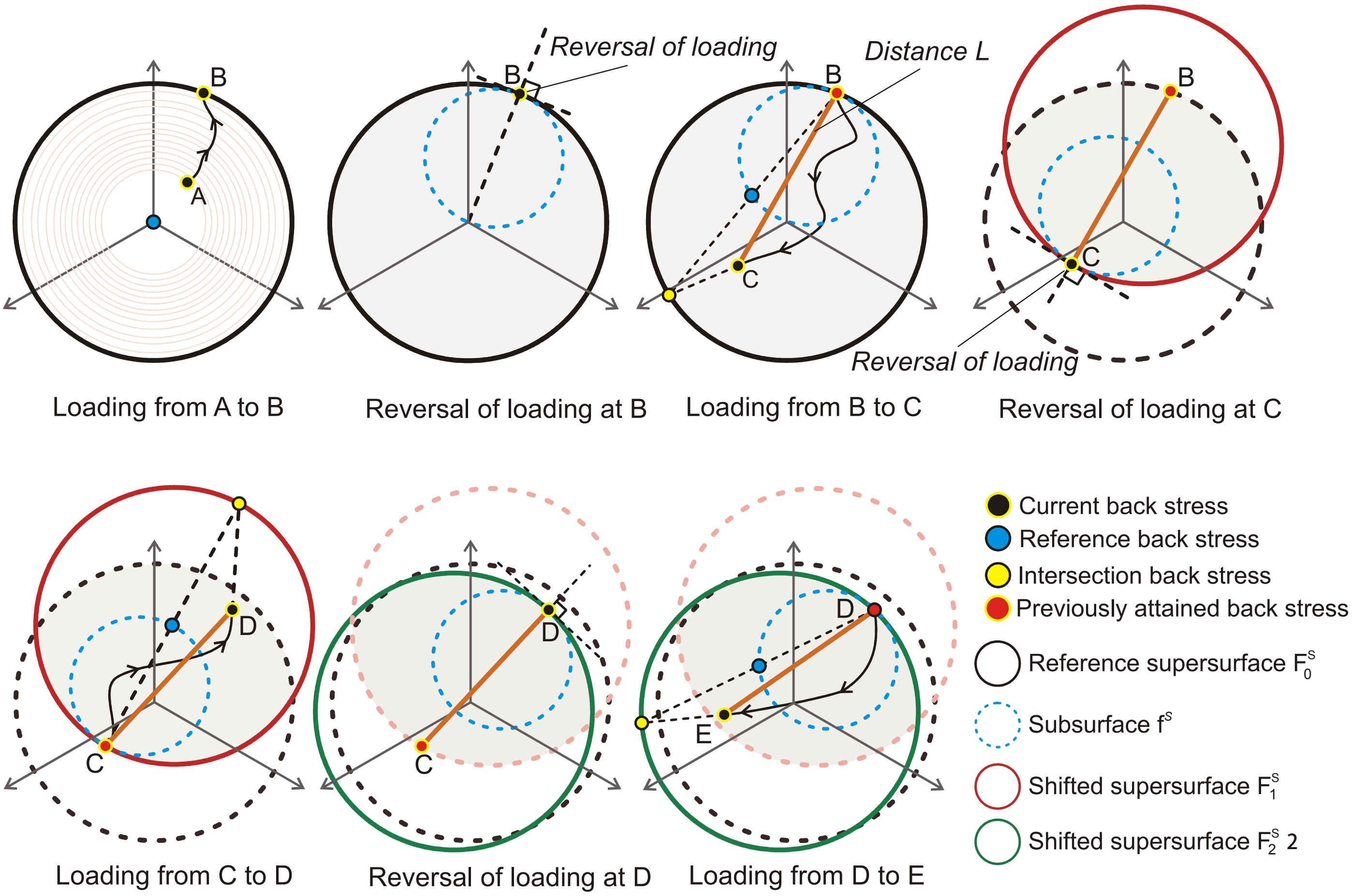

Fig. 12 – Multiaxial representation of the model behavior

To find the intersection point, parameter β should be put back into the line equation (35). The intersection tensor Z_{ij} is then defined as:

$$Z_{ij} = X_{ij} + n_{ij}\beta \tag{39}$$

The expression (39) contains variables, which show stepwise dependency such that they changes value only with reversal of the load path. To form an evolution equation for these variables in terms of the delta function, the condition of the reversal of loading paths is formulated. As the case of uniaxial unloading may not exist in multiaxial case, the load reversal condition is defined in terms of the shortest distance between current back stress and previously attained back stress. The critical distance is defined as:

$$L = \sqrt{\frac{3}{2}\left(X_{ij} - \bar{X}_{ij}\right)\left(X_{ij} - \bar{X}_{ij}\right)} \tag{40}$$

Load reversal occurs when the distance L stops growing, such that $\dot{L} = 0$. This condition can be directly inserted into the evolution equations for variables with stepwise dependency:

$$\dot{\chi} = \delta\left(G^x\right)\frac{\dot{G}^x}{\dot{p}} f\left(p, \chi\right)\dot{p} \tag{41}$$

where G^x is a kernel of the delta function. Condition (41) means that when G^x is equal to zero, the delta function gives an instant change for a variable χ on the value of $f\left(p, \chi\right)$. To fulfil the condition of loading reversal, G^x is written in the form:

$$G^x = \frac{\dot L}{\dot p} + \left| \frac{\dot L}{\dot p} \right| \tag{42}$$

The use of (42) allows instant change of a variable for cases of both smooth and sharp dependencies of L on p as shown in Fig. 13. The full derivative of $\dot L / \dot p$ can be calculated analytically:

$$\frac{\dot L}{\dot p} = \frac{\partial L}{\partial p} + \frac{\partial L}{\partial X_{ij}} \frac{\dot X_{ij}}{\dot p} = \frac{2}{3} \frac{X_{ij} - \bar X_{ij}}{L} AB \exp\left(-\frac{2}{3} \frac{\left(X_{kl} - O_{kl} \right) n_{kl}}{B} \right) n_{ij} \tag{43}$$

The evolution rule for $\bar X_{ij}$ is then written as:

$$\dot{\bar X}_{ij} = \delta\left(G^x \right) \frac{G^{\dot x}}{\dot p} [X_{ij} - \underset{\leftarrow}{\bar X}_{ij}] \dot p \tag{44}$$

where $\underset{\leftarrow}{\bar X}_{ij}$ is previously attained back stress tensor which is defined at a previous moment of time with a time delay τ :

$$\underset{\leftarrow}{\bar X}_{ij} = \bar X_{ij} \left(t - \tau \right) \tag{45}$$

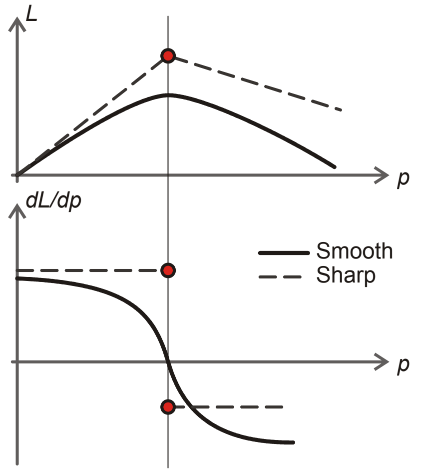

Fig. 13 – Smooth and sharp dependence of L parameter on accumulated plastic strain

Introduction of a time delay in equation (44) is required to avoid uncertainty at a moment of load reversal when the argument of the delta function takes zero value. The value of variable $\bar X_{ij}$ at a new step of loading depends on its value from a previous loading step defined before reversal of loading, as shown in Fig. 14. An instant change of the variable $\bar X_{ij}$ therefore depends on its value at any moment of time before reversal of loading. Subsequently, the time delay must be a value smaller than the value of the step duration itself.

Referring to Fig. 11b, with a new reversal of the loading path at point C loading proceeds to point D. Figure 11b suggests that if reversal occurs within the reference supersurface F_0^s, the Curve 2 from the hysteresis loop always tends to close the loop with Curve 1. In fact, Curve 2 shares the same hardening as of Curve 1 with another position of reference back stress. In the general stress state, another surface called shifted supersurface F_1^s is created at the reversal point C. It is assumed that the hardening laws inside F_1^s is the same as inside F_0^s, but relatively a new position of reference back stress. The shifted supersurface F_1^s is written as:

$$F_1^s=\sqrt{\frac{3}{2}\left(X_{ij}-\bar{c}_{ij}^{s1}\right)\left(X_{ij}-\bar{c}_{ij}^{s1}\right)}-R_s \tag{46}$$

where $\bar{c}_{ij}^{s1}$ is coordinates of the centre.

The supersurface is able to move instantly only at the reversal of loading step and remains unchanged during loading. It also keeps the same radius R^s as the reference supersurface F_0^s. Figs 10a, 10b and 10c show that the centre of the supersurfaces coincides with the shift point. However, this is only valid for the case of proportional loading. To develop a general evolution rule for the supersurface centre and reference back stress tensor, a general case of multiaxial loading is considered in Fig. 12 as loading from point C to point D.

In the case of loading reversal from the reference supersurface F_0^s at point B, the reversal at point C occurs when the shortest distance between current back stress and previously attained back stress stops growing, such that $\dot{L}=0$. As the supersurface F_1^s is created at the reversal point C with tangent plane perpendicular to the distance L, the evolution equation of centre of the shifted supersurface F_1^s is formulated in terms of the delta function:

$$\dot{\bar{c}}_{ij}^{s1}=\delta\left(G^x\right)\frac{\dot{G}^x}{\dot{p}}\left[\frac{R_s}{\underleftarrow{L}}\left(X_{ij}-\overline{\underleftarrow{X}}_{ij}\right)+\overline{\underleftarrow{X}}_{ij}-\underleftarrow{\bar{c}}_{ij}^{s1}\right]\dot{p} \tag{47}$$

where $\underleftarrow{\bar{c}}_{ij}^{s1}$ is centre of the supersurface defined at a previous moment of time with a time delay τ:

$$\underleftarrow{\bar{c}}_{ij}^{s1}=\bar{c}_{ij}^{s1}\left(t-\tau\right) \tag{48}$$

and $\underleftarrow{L}$ is defined as:

$$\underleftarrow{L}=\sqrt{\frac{3}{2}\left(X_{ij}-\overline{\underleftarrow{X}}_{ij}\right)\left(X_{ij}-\overline{\underleftarrow{X}}_{ij}\right)} \tag{49}$$

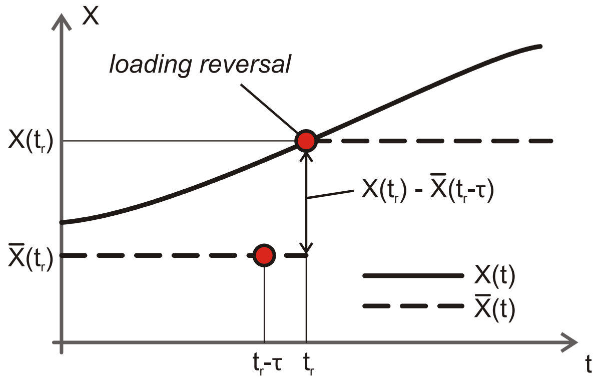

Fig. 14 – Evolution of back stress and previously attained back stress

To further define the deformation process, a new reversal at point D is considered. It is shown in Figure 11c that a new Curve 3 shares the same hardening as from Curve 1 and Curve 2. In terms of multiaxial loading case, another shifted supersurface F_2^s is created when the distance L stops growing as shown in Figure 12. The definition of this supersurface F_2^s is the same as for F_1^s:

$$F_2^s = \sqrt{\frac{3}{2}\left(X_{ij} - \bar{c}_{ij}^{s2}\right)\left(X_{ij} - \bar{c}_{ij}^{s2}\right)} - R_s \tag{50}$$

where the centre $\bar{c}_{ij}^{s2}$ of the supersurface defined as:

$$\dot{\bar{c}}_{ij}^{s2} = \delta\left(G^x\right)\frac{\dot{G}^x}{\dot{p}}\left[\frac{R^s}{\underleftarrow{L}}\left(X_{ij} - \underleftarrow{\bar{X}}_{ij}\right) + \underleftarrow{\bar{X}}_{ij} - \underleftarrow{\bar{c}}_{ij}^{s2}\right]\dot{p} \tag{51}$$

Hardening inside F_2^s is the same as inside F_1^s, however with different position of reference back stress tensor. It is important to note that a new reversal inside the shifted supersurface F_2^s at point E does not create a new shifted supersurface, but the shifted supersurface F_1^s will be moved instantly to a new position defined by the equation (51).

To generalize this point, every new reversal inside shifted supersurface F_2^s instantly moves shifted supersurface F_1^s and every reversal inside shifted supersurface F_1^s instantly moves the shifted supersurface F_2^s. To prove this assumption, a test with loading program shown in Fig. 15a is performed. The stress-strain response of this loading is shown in Fig. 15b and Fig. 15c. The use of this type of loading provides that every new reversal of loading occurs within one of shifted supersurface F_1^s or F_2^s. Curve 2 consists of two parts: the first one is before the transition point with reference Point 2 and the second one is after the transition point with reference Point 1. It can be concluded that with crossing the boundary of the shifted supersurface F_1^s at the transition point, the reference Point 1 moves to reference Point 2 and Curve 2 continues with the same hardening as of Curve 1 from the first step of loading. The fact that Curve 2 does not follow hardening of Curve 3 with reference Point 3 means that with crossing the boundary of the shifted supersurface F_1^s, the loading state does not come back into the previous shifted supersurface but returns back inside the reference supersurface F_0^s. As a conclusion, only two shifted supersurfaces which alter between each other whenever reversal of loading occurs are enough to describe the loading process and history of plastic deformation.

To describe the deformation process with switching between the two supersurfaces, switching operators $\mathbb{N}_1$ and $\mathbb{N}_1$ are introduced as:

$$\dot{\mathbb{N}}_1 = \delta(G^x)\frac{G^{\dot{x}}}{\dot{p}}\left[1 - H(F_0^s)\right]\left(\underrightarrow{\mathbb{N}}_2 - \underrightarrow{\mathbb{N}}_1\right)\dot{p} \tag{52}$$

$$\dot{\mathbb{N}}_2 = \delta(G^x)\frac{\dot{G}^x}{\dot{p}}\left[1 - H(F_0^s)\right]\left(\underrightarrow{\mathbb{N}}_1 - \underrightarrow{\mathbb{N}}_2\right)\dot{p} \tag{53}$$

The evolution equations for the shifted supersurfaces F_1^s and F_2^s and coefficient β are then modified as:

$$\dot{\bar{c}}_{ij}^{s1} = \delta\left(G^x\right)\frac{\dot{G}^x}{\dot{p}}\left[\frac{R^s}{\underleftarrow{L}}\left(X_{ij} - \underleftarrow{\bar{X}}_{ij}\right) + \underleftarrow{\bar{X}}_{ij} - \underleftarrow{\bar{c}}_{ij}^{s1}\right]\mathbb{N}_1\dot{p} \tag{54}$$

$$\dot{\bar{c}}_{ij}^{s2} = \delta\left(G^x\right)\frac{\dot{G}^x}{\dot{p}}\left[\frac{R^s}{\underleftarrow{L}}\left(X_{ij} - \underleftarrow{\bar{X}}_{ij}\right) + \underleftarrow{\bar{X}}_{ij} - \underleftarrow{\bar{c}}_{ij}^{s2}\right]\mathbb{N}_2\dot{p} \tag{55}$$

$$\beta = \frac{-\mu_2 \pm \sqrt{\mu_2^{\,2} - 6\mu_3}}{3} \tag{56}$$

where coefficients of the quadratic equation μ_2 and μ_3 are determined as:

$$\begin{aligned} \mu_2 &= 2n_{ij}\left(X_{ij} - \bar{c}_{ij}\right) \\ \mu_3 &= \left(\bar{c}_{ij}^{s1}\mathbb{N}_1 + \bar{c}_{ij}^{s2}\mathbb{N}_2 - X_{ij}\right)\left(\bar{c}_{ij}^{s1}\mathbb{N}_1 + \bar{c}_{ij}^{s2}\mathbb{N}_2 - X_{ij}\right) - \frac{2}{3}R_s^{\,2} \end{aligned} \tag{57}$$

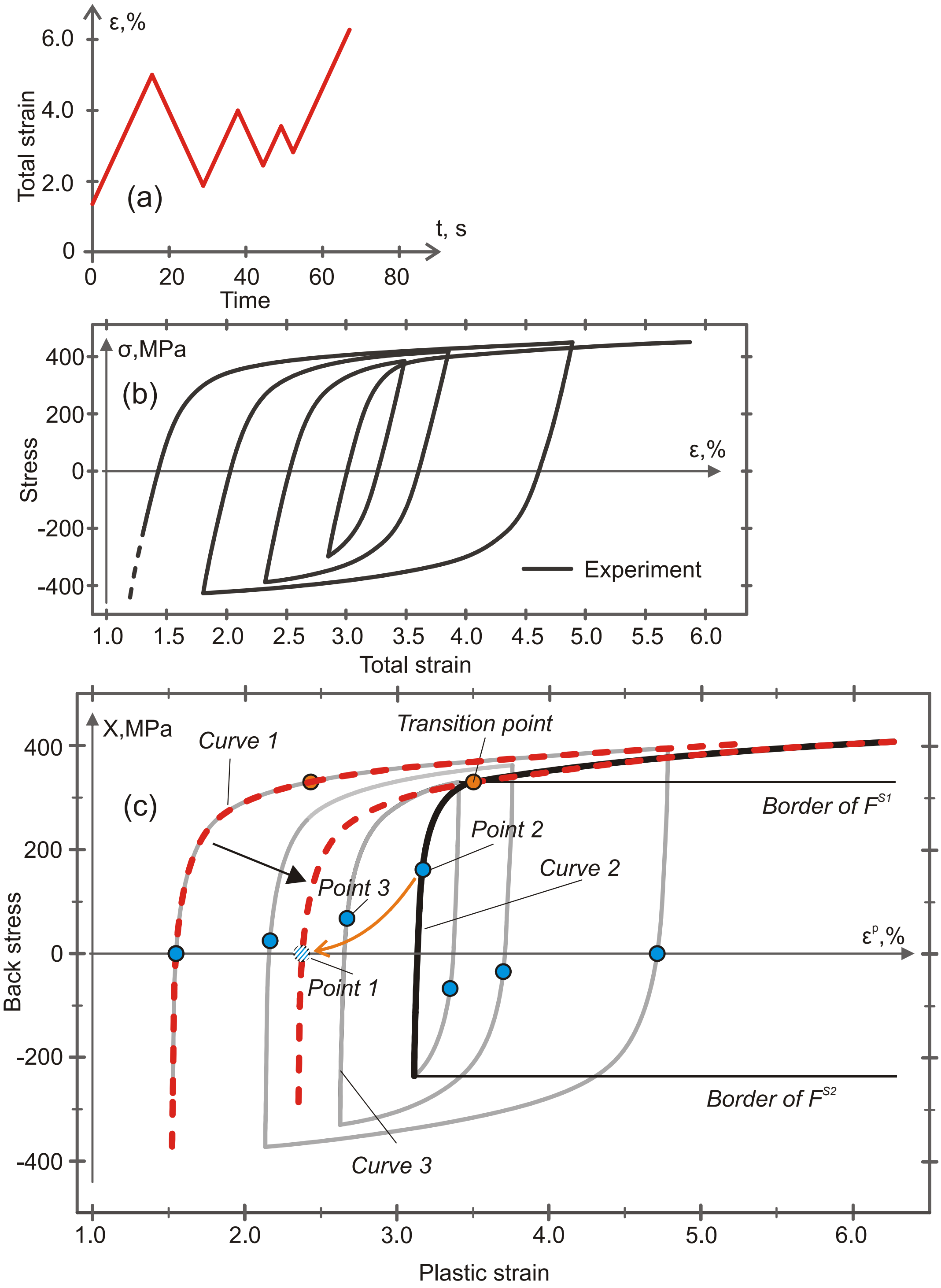

Fig. 15 – Testing with loading to define number of supersurfaces; (a) loading program , (b) stress vs. total strain and (c) back stress vs plastic strain

8.2 Case 2

Another reason for the shift of deformation curves is transition between curves such as from Curve 3 to Curve 1 in Fig. 8. This situation means that current stress crosses the boundary of one of the supersurfaces and the reference point relaxes to zero value without reversal of load. To modify the equation for the back stress shift tensor, a new parameter μ responsible for the transition between deformation curves is introduced into the equation of back stress reference tensor:

$$O_{ij} = \frac{1}{2}\mu\left(Z_{ij} - \bar{X}_{ij}\right) \tag{58}$$

Parameter μ should be equal to one whenever the loading is inside of all of the three supersurfaces and takes zero once current stress approaches the boundary of one of the supersurface. Evolution equation for parameter μ for the case when the current stress approaches the boundary of the shifted supersurface F_1^s is formulated as:

$$\dot{\mu} = \delta\left(F_1^s\right)\dot{F}_1^s \tag{59}$$

or in terms of accumulated plastic strain rate as:

$$\dot{\mu} = \delta\left(F_1^s\right)\frac{\dot{F}_1^s}{\dot{p}}\dot{p} \tag{60}$$

While moving inside of one of the supersurface the current stress can cross the border of any of the supersurface leading to relaxation of the reference point. Therefore the parameter μ should include the condition for relaxation for the three cases of crossing the boundary. Once the boundary is crossed, the parameter μ is equal to zero. A new reversal of loading should return it to one. To include these requirements into the evolution equation, the following modifications are made:

$$\dot{\mu} = \left(-h\sum_{i=0}^{2}\delta\left(F_i^s\right)\frac{\dot{F}_i^s}{\dot{p}} + \delta(G^x)\frac{\dot{G}^x}{\dot{p}}H(-\mu)\right)\dot{p} \tag{61}$$

$$h = \left[1 - H\left(F_0^s\right)\right]H\left(-F_1^s\right)H\left(-F_2^s\right) \tag{62}$$

Once one of the supersurfaces is crossed, the deformation process continues with the stress state inside or on the reference supersurface further evolving the reference supersurface. Solution of equation (61) for uniaxial loading provides an instant relaxation of the reference point such that Curve 3 closes the loop with Curve 1. However, in the real behavior of the material, there is no closed loop such that a deviation effect occurs when stress approaches the upper point of the hysteresis loop, inducing a ratcheting phenomenon. This behavior will be discussed in the companion paper (Part II), where an approximate form of the Dirac delta function is used for modelling the deviation effect.

9. Non-proportional hardening

The proposed model of kinematic hardening in the form (19) evolves back stress only in the direction of plastic strain. This behaviour has been observed experimentally but only for proportional loading. Lamba and Sidebottom (1978) demonstrated that better agreement with experimental results of non-proportional loading is achieved when back stress can evolve in a different direction according to the Mróz (1967) kinematic hardening model. In A-F models, the directionality is provided by the dynamic recovery term, which pulls the back stress towards the centre of the coordinate system in the deviatoric stress space.

In this study, the proposed kinematic hardening rule (19) is modified to include dynamic recovery in the following way:

$$\dot{X}_{ij} = AB\exp\left(-\frac{2}{3}\frac{X_{kl}n_{kl}}{B}\right)\dot{\varepsilon}^{p}_{ij} - \gamma\left(X_{ij} - \frac{2}{3}X_{kl}n_{kl}n_{ij}\right)\dot{p} \qquad (63)$$

where γ is a material constant. The term $\frac{2}{3}\gamma X_{kl}n_{kl}n_{ij}\dot{p}$ is a projection of the increment of back stress $\dot{X}_{ij} = -\gamma X_{ij}\dot{p}$ on the yield surface normal n_{ij} (Fig. 16). Equation (63) implies that the second term in the right hand side comes into play only when non-proportional loading occurs. For any proportional loading, with a coincident direction of the yield surface normal n_{ij} and back stress radios vector $\overline{r}_{ij}$, the second term is cancelled out. By subtracting the projection of the back stress increment $\frac{2}{3}\gamma X_{kl}n_{kl}n_{ij}\dot{p}$, it is ensured that the back stress increment along the yield surface normal is defined by the first term in the right hand side of equation (63). The second term therefore affects only non-proportional loading, depending on the scalar product $X_{kl}n_{kl}$. It is noted that ~~in this study,~~ proportional loading during plastic deformation occurs whenever the back stress radios vector $\overline{r}_{ij}$ coincides with or opposite in direction to the yield stress normal n_{ij} in the deviatoric stress space.

Equation (63) is a convenient way of representing the directional behaviour of the back stress evolution, as the increment of back stress due to non-proportional hardening does not interact with proportional hardening. This allows more flexibility in modelling non-proportional hardening responses, as shown for simulation examples of model application presented in the companion paper, Part II, where for the same proportional stress-strain curve, different nonproportional responses are simulated depending on the material constant γ. As the non-proportional loading term of equation (63) does not interact with the proportional one, all subsequent model developments presented in this study are written for the case of proportional loading only. The non-proportional term can always be added if required.

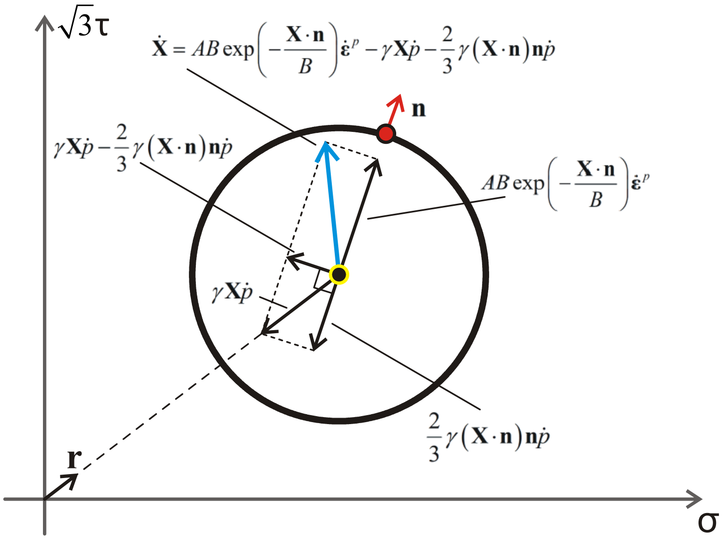

Fig. 16 – Representation of kinematic hardening rule (63)

10. Transition from the initial stress-strain curve

For many metals the shape of initial stress-strain curve is different from the subsequent curves of cyclic loading. Figure 2 demonstrates a typical stress-strain response for carbon steels where the initial stress-strain curve has a plateau. It is seen that initial monotonic stress-strain curve is different from other curves and cannot be approximated by the same hardening law as other curves directly.

The occurrence of a plateau during monotonic loading is known as the Luder's band phenomenon, which is highly localised plastic deformation of single crystals. Jiang (2001); Zhang and Jiang (2005a, 2005b) presented experimental evidence of the localised nature of the plastic deformation of the plateau, as well as cyclic deformation in general, for 1045 steel under uniaxial and multiaxial loading conditions. The experimental procedure included force and strain controlled cyclic loading tests, where strain was measured by means of a standard extensometer and local strain gauges located along the gauge section of the specimens. The measurements showed that the local strains from the strain gauges are all different from the extensometer strain for monotonic deformation on the plateau, due to the localised nature of the Luder's band phenomenon. The difference persists for subsequent strain hardening regions and during cyclic loading. However, an average value of stain calculated from all measurements of the local stain gauges were seen to be close to the extensometer strain measurement. This indicates that the bulk behaviour of structures can be approximately described using experimental inputs of engineering stress-strain responses obtained by means of extensometer measurement, not only for strain hardening behaviour, as widely used in practice, but also for phenomenological description of the plateau behaviour. Such an approach is used by Ucak and Tsopelas (2011, 2012) to describe the plateau behaviour of carbon steels, where the concept of Chaboche nonlinear hardening is coupled with an introduced pseudo memory surface. The bounding surface initially coincides with the yield surface and is not allowed to translate and expand. Specific nonlinear hardening rules are defined inside and on the bounding surface, such that loading-on and unloading-from the plateau are properly simulated. The boundary surface vanishes when a condition for exiting the plateau region is satisfied.

This study attempts to describe transition between the initial monotonic and subsequent stress-strain curves by a unified set of differential equations with the same kinematic hardening rule and the same set of material constants. To extend the developed evolution rules for cyclic plastic deformation for the case of cyclic loading with the plateau, a few test with different loading programs were performed. Figures 17a, 17b, 17c and 17d show stress-strain curves after tension-compression tests with different loading programs. An important observation here is that regardless of loading direction and program the material must undergo a certain value of plastic strain $\hat{\varepsilon}$ before hardening occurs. Figure 17a suggests that the value of $\hat{\varepsilon}$ is the same for tensile and compression load and for both cases the plateau occurs at the same stress magnitude of 255 MPa. Figure 3.15b shows that the sum of plastic strain which was accumulated during loading at the plateau for tensile load following compression load is equal to $\hat{\varepsilon}$. It is also found that plastic strain accumulated during cycling with loading below σ_y does not change the value of $\hat{\varepsilon}$ such that once the value of σ_y is attained hardening occurs only after plastic strain has accumulated the value of $\hat{\varepsilon}$ (Figure 17b). Initial plastic flow starts before the stress reaches the value of σ_y when the plateau initiates as established in Figure 2. It occurs when stress exceeds the value of σ_0 and continues until the initiation of the plateau. This observation suggests existence of a stress surface inside which plastic deformation with large hardening can occur. Once the stress state is on the surface, plastic deformation occurs with no hardening until accumulated plastic strain has the value of $\hat{\varepsilon}$. It is convenient to associate this surface with already introduced reference supersurface F_0^s:

$$F_0^s = \sqrt{\frac{3}{2} X_{ij} X_{ij}} - R_s - X_y \tag{64}$$

where X_y is back stress yield point defined from uniaxial tensile or compression tests which corresponds to initiation of the plateau.

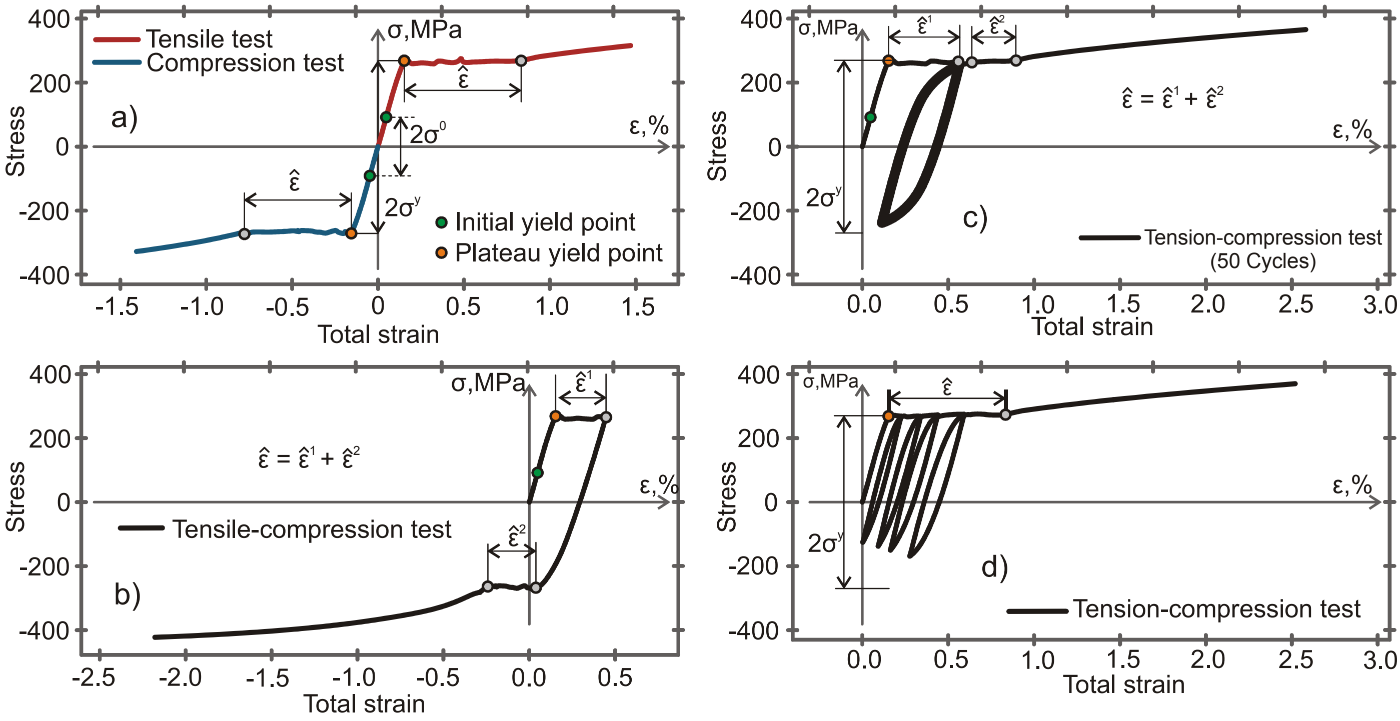

Fig. 17 – Plateau behavior of S355J2 steel during (a) one step of tensile and compression, (b) tensile following by compression, (c) cyclic below plateau stress and (d) ratcheting below the plateau

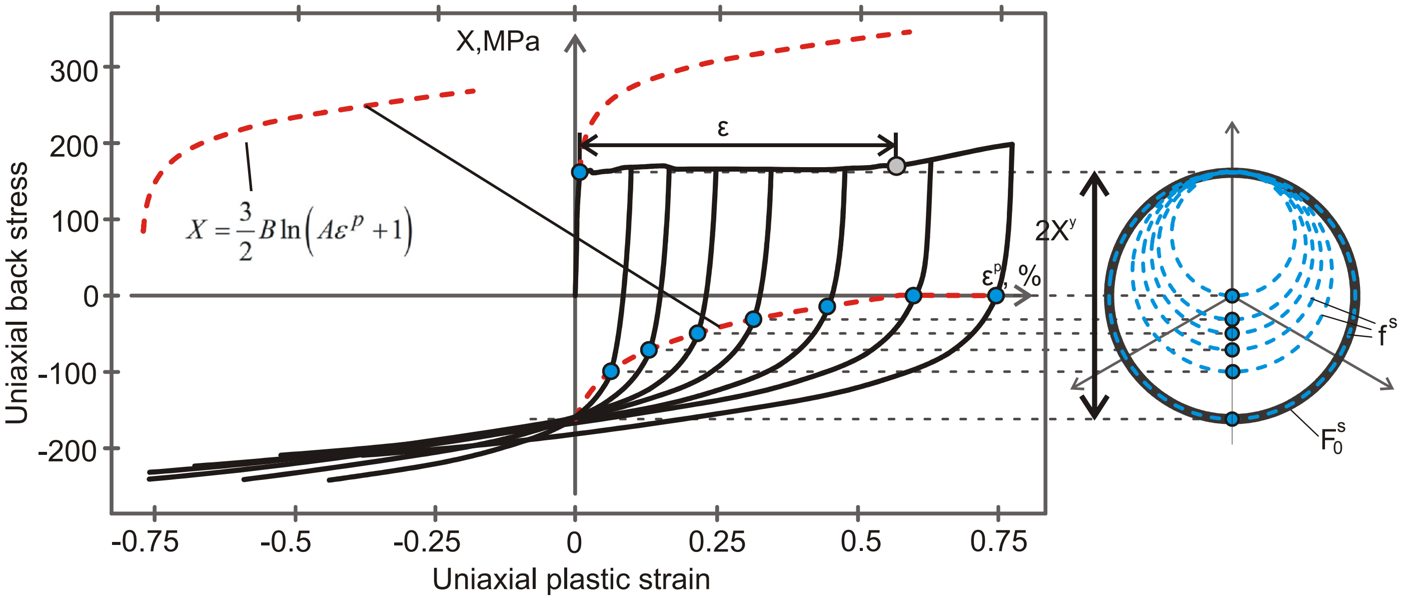

Fig. 18 – Modelling of the plateau

To define the evolution rule for the back stress shift tensor for loading inside the supersurface, several loading-unloading tests were performed. Figure 18 suggests that the initial hardening of the material before the stress state reaches the yield point can be described with the stress-strain relationship defined by the developed kinematic hardening rule (25) with a shift point which coincides with the back stress yield point. That means the reference supersurface F_0^s coincides with subsurface f^s in the initial state. When load reversal occurs on the plateau, the shift point has a non-zero value. Once the plateau region is passed and hardening occurs, reversal compression curves have a reference point equal to zero. This means the back stress shift tensor has a different evolution rule when loading is inside and on the reference supersurface.

Figure 18 shows that during reversal of loading to compression from the plateau, the reference points are changed according to the logarithmic function (20). Therefore, it is convenient to introduce a variable which is responsible for the back stress shift during loading below and on the plateau associated with the hardening law as:

$$\dot{X}_h = \frac{3}{2}AB\left(1-C\right)\exp\left(-\frac{2}{3}\frac{X_h}{B}\right)\dot{p} \tag{65}$$

where parameter C is defined as follows:

$$C = 1 - H\left(F_0^s\right)\left[1 - H\left(2X_h - X_y\right)\right] \tag{66}$$

The combination of Heaviside functions in (66) means that when loading is on the reference supersurface F_0^s defined by $H\left(F_0^s\right)$ and X_h has not reached the value of X_y defined by $\left[1 - H\left(X_h - X_y\right)\right]$, C is equal to zero and X_h develops according to (65).

Once loading is inside the main supersurface or X_h exceeds the value of X_y, C is equal to one and X_h stays unchanged. It should be noted that attaining the value of X_y by X_h is equivalent for accumulated plastic strain p to reach the value of $\hat{\varepsilon}$ while loading on the plateau. The definition of $\hat{\varepsilon}$ is also similar to plateau region strain defined in (Ucak and Tsopelas, 2011, 2012).

The kinematic hardening rule is modified to the following form:

$$\dot{X}_{ij} = ABC\exp\left(-\frac{2}{3}\frac{\left(X_{kl} - O_{kl}\right)n_{kl}}{B}\right)\dot{\varepsilon}_{ij}^{p} \tag{67}$$

The modified expression of the kinematic hardening law ensures that when stress reaches the yield point, the plateau begins with no hardening. Once unloading starts from the plateau, hardening occurs with the back stress shift defined by O_{ij}. Finally, when X_h exceeds the value of X_y, C is equal to one and loading is defined by the developed hardening rules.

To ensure that the reference supersurface F_0^s develops only when loading leaves the plateau, the evolution rule of the radius R_s should also be modified:

$$\dot{R}_s = H\left(F_0^s\right)H\left(2X_h - X_y\right)\frac{\dot{X}_{eq}}{\dot{p}}\dot{p} \tag{68}$$

Finally, the evolution rule for the back stress shift tensor that describes all deformation process including initial hardening, plateau and subsequent deformation is updated to:

$$O_{ij} = \frac{2X_y - X_h}{2X_y}\mu\left(Z_{ij} - \bar{X}_{ij}\right) \tag{69}$$

Generalising the case of loading with the plateau for multiaxial loading conditions based on the developed form for the back stress reference tensor (69) suggests that the initial reference supersurface F_0^s and subsurface f^s coincide as shown in Fig. 18. With loading on the plateau, the subsurface decreases its size for the direction of plastic deformation based on the evolution rule (65). Finally, when the diameter of the subsurface becomes equal to the radius of the reference supersurface, loading leaves the plateau region and deformation continues with kinematic hardening.

11. Isotropic hardening compensation

Materials usually exhibit combined isotropic and kinematic hardening such that the yield surface can move and change its size. It has been established experimentally here that in the case of S355J2 steel the larger part of the deformation process is described by kinematic movement of the yield surface and the smaller part of isotropic hardening occurs when the initial size of the yield surface is decreased, as shown in Fig. 3d. To fully associate the uniaxial stress-strain curve shape with the kinematic hardening model, it is convenient to include the isotropic part of deformation hardening described by the equation (7) into the rule of kinematic hardening as shown in Fig. 19 in the form:

$$X_{ij}^{T} = X_{ij} + X_{ij}^{R} \tag{70}$$

where X_{ij}^{R} is kinematic hardening responsible for compensation of the isotropic hardening part and is written:

$$\dot{X}_{ij}^{R} = -n_{ij}\dot{R} \tag{71}$$

This separation is convenient, because all deformation process defined by uniaxial stress-strain curves can be calibrated directly to the developed kinematic hardening rule for the component X_{ij}. In the case of uniaxial tensile loading, the integration of kinematic and isotropic hardening rules gives:

$$\sigma = X + R + X^{R} + \sigma_0 \tag{72}$$

Positive X^{R} cancels out negative R giving: $\sigma = X + \sigma_0$. The yield surface is then modified to the following form:

$$f = \sqrt{\frac{3}{2}\left(S_{ij} - X_{ij}^{T}\right)\left(S_{ij} - X_{ij}^{T}\right)} - R - \sigma_0 \tag{73}$$

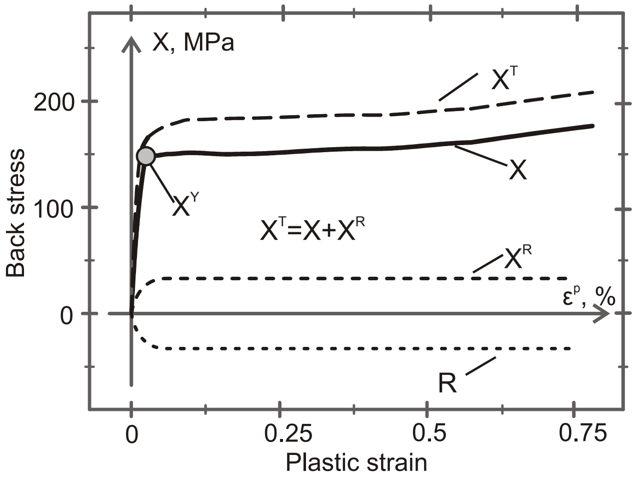

Fig. 19 – Representation of isotropic hardening compensation

12. Elastic-plastic transition during unloading

Figure 20a and Figure 20b shows the results of stress-strain slope modulus measurement during unloading stages, with reduction of up to 20% of initial value of the chord modulus. There are several modelling concepts to take into account variations of the unloading curve modulus during plastic deformation. They can be divided into two main groups of linear and nonlinear modeling of elastic modulus. With linear modelling, Young's modulus is represented as a chord modulus, which is a linear slope defined by a line connecting two points of an unloading stress-strain curve. Conventionally, these points are the stress where unloading starts and zero stress which corresponds to the unloaded state. Unloading slope is then defined as a function of plastic pre-strain $E_{chord} = g(\bar{\varepsilon}^p)$. As an example, exponential form developed by Yoshida et al. (2002) can be used:

$$E_{chord} = E_i - \left(E_i - E_a\right)\left[1 - \exp\left(-\zeta\bar{\varepsilon}^p\right)\right] \tag{74}$$

where E_i is initial chord modulus, E_a is chord modulus after large plastic pre-strain and ζ is a material parameter.

As behavior of the material during unloading stage is known to be nonlinear, Chen et al. (2016); Sun and Wagoner (2011) proposed the following nonlinear equation for an unloading stress-strain curve:

$$E = \begin{cases} E_o & \text{for } \Delta\varepsilon \le \varepsilon_c \\ E_o - A_1\left[1 - \exp\left(-A_2\left(\Delta\varepsilon - \varepsilon_c\right)\right)\right] & \text{for } \Delta\varepsilon > \varepsilon_c \end{cases} \tag{75}$$

where $\Delta\varepsilon$ is the absolute value of the increment of strain from the unloading path; ε_c is a value of critical transition strain which separates linear and nonlinear portions of deformation; A_1 and A_2 are material parameters.

With the use of equation (75) the deformation process is divided into three stages. The first stage is elastic loading until the strain increment $\Delta\varepsilon$ reaches the value of ε_c. After that, loading continues as quasi-elastic-plastic (QPE) with unloading slope defined by (75) for $\Delta\varepsilon > \varepsilon_c$ up to the stage of normal plastic deformation after exceeding conventional yield stress.

To provide consistent modelling of quasi-elastic-plastic deformation, the framework of introducing additional yield surfaces should be used. However, this may complicate a material modelling approach. As an alternative to the approach of quasi-elastic-plastic deformation, it is proposed to use the nonlinear kinematic hardening rule developed in this study. This model naturally accounts for variation of hardening slope for an unloading stress-strain curve starting from points of early yielding. This is achieved by the property of the hardening rule during reversal of the loading path. According to the developed model, the hardening slope during tensile plastic pre-strain is expressed as:

$$E_p = \frac{dX}{d\varepsilon^p} = \frac{3}{2}AB\exp\left(-\frac{2X}{3B}\right) \tag{76}$$

With loading reversal at point X_0, the hardening slope changes to $E_p = \frac{3}{2}AB\exp\left(\frac{2X_0}{3B}\right)$. With the use of small offset yield stress definition, this slope is usually several orders magnitudes harder than the elastic slope of the material $E_p \gg E_i$, meaning that the total slope at point X_0 is:

$$E_T = \frac{E_p E_i}{E_p + E_i} \approx E_i \tag{77}$$

With continuation of plastic deformation to the point of zero stress, the slope gradually develops to the value of:

$$E_T = \frac{ABE_i}{AB + \frac{2}{3}E_i} \tag{78}$$

As shown in Fig. 20c, the proposed nonlinear kinematic hardening model predicts the unloading stress-strain curve with reasonable accuracy when compared with the QEP model and other unloading modulus definitions. The hardening property of the model provides a gradual transition between elastic and elastic-plastic regions at the yield point with small plastic strain offset.

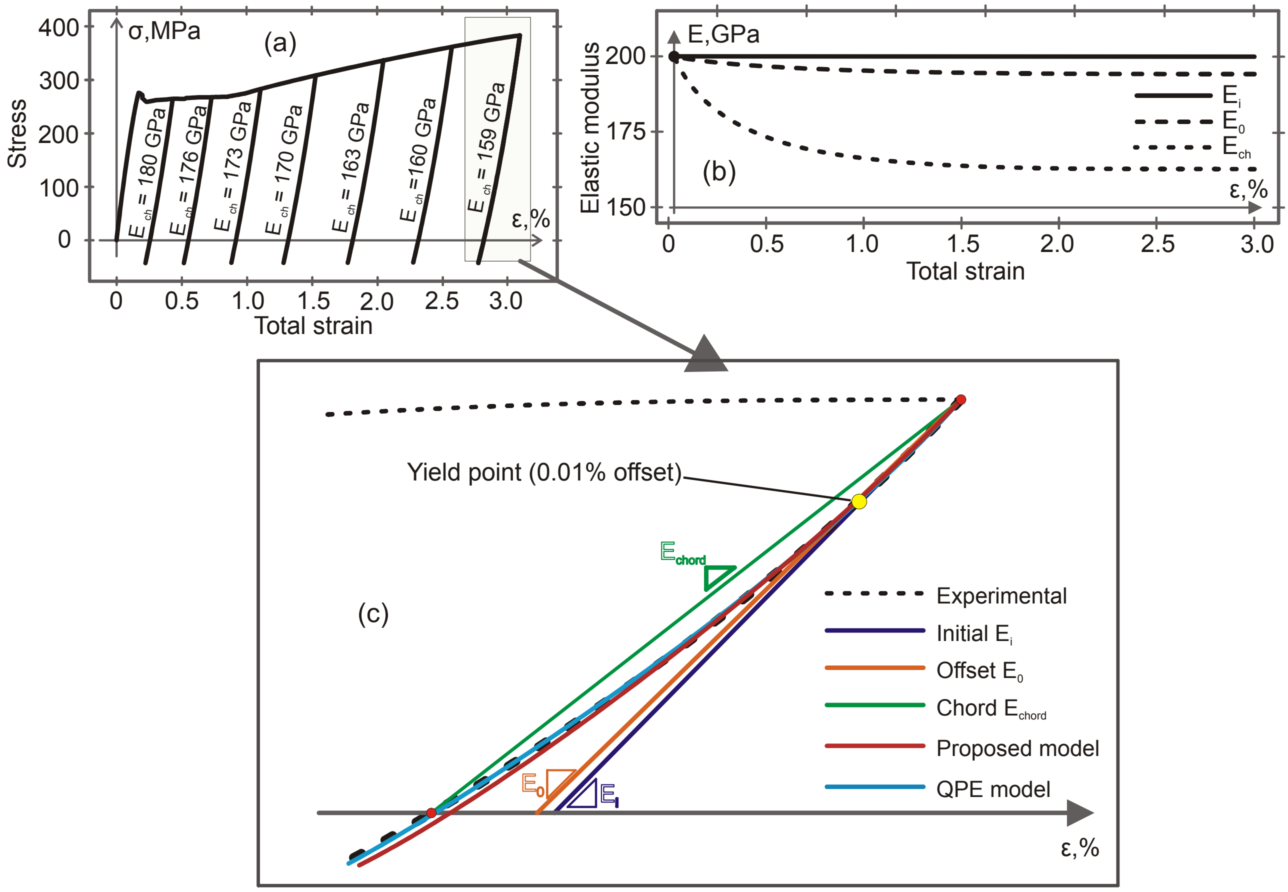

Fig. 20 – Variation of unloading slopes of S355J2 steel; (a) Measurement of chord modulus during loading-unloading, (b) measured unloading modulus vs. plastic pre-strain and (c) modelling with different models

13. Effect of hydrostatic pressure

It is observed in many metals that cyclic plasticity deformation curves have different hardening slopes for tensile and compression loading (Voyiadjis et al., 2012). Such difference is significant for notched samples with high hydrostatic pressure. As hydrostatic pressure is present during the uniaxial tension-compression stress state, its effect on stress-strain curves is also expected. Figure 21 shows the uniaxial monotonic stress-strain curves obtained for both tensile and compression tests for S355J2 steel. It is shown that uniaxial compression curve has a steeper stress-strain slope. The difference in hardening was also found during subsequent loading cycles, as shown in Fig. 22 for the case of stabilised stress-strain hysteresis loops under two different strain ranges for the investigated S355J2 steel (Fig. 22a). This material behaviour is also present in 304 stainless steel (Kang et al., 2003) (Fig. 22b) and 2124-T851 aluminum alloy (Halama et al., 2017) (Fig. 22c). Voyiadjis et al. (2012) proposed modelling the effect of different hardening through the influence of the first stress invariant on the parameter of isotropic hardening as:

$$R = \left[Q_1 + Q_2 \exp\left(-b_1 I_1\right)\right]\left(1 - \exp\left(-b_2 p\right)\right) \tag{79}$$

where Q_1, Q_2, b_1 and b_2 are material parameters and I_1 is the first stress invariant defined as $I_1 = \sigma_{ii}$.

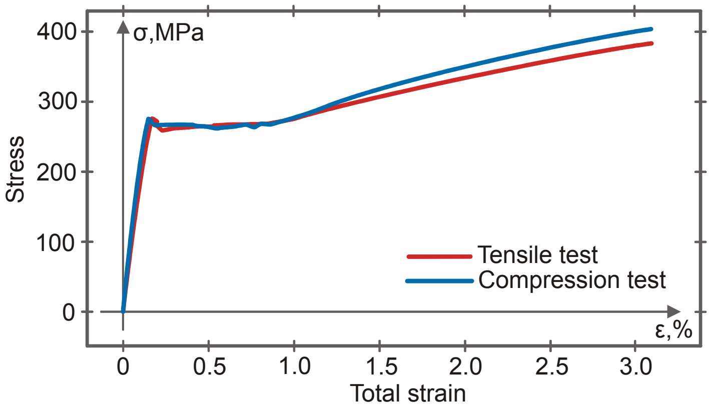

Fig. 21 – Difference between tensile and compression stress-strain curves of S355J2 steel (absolute stress values for compression)

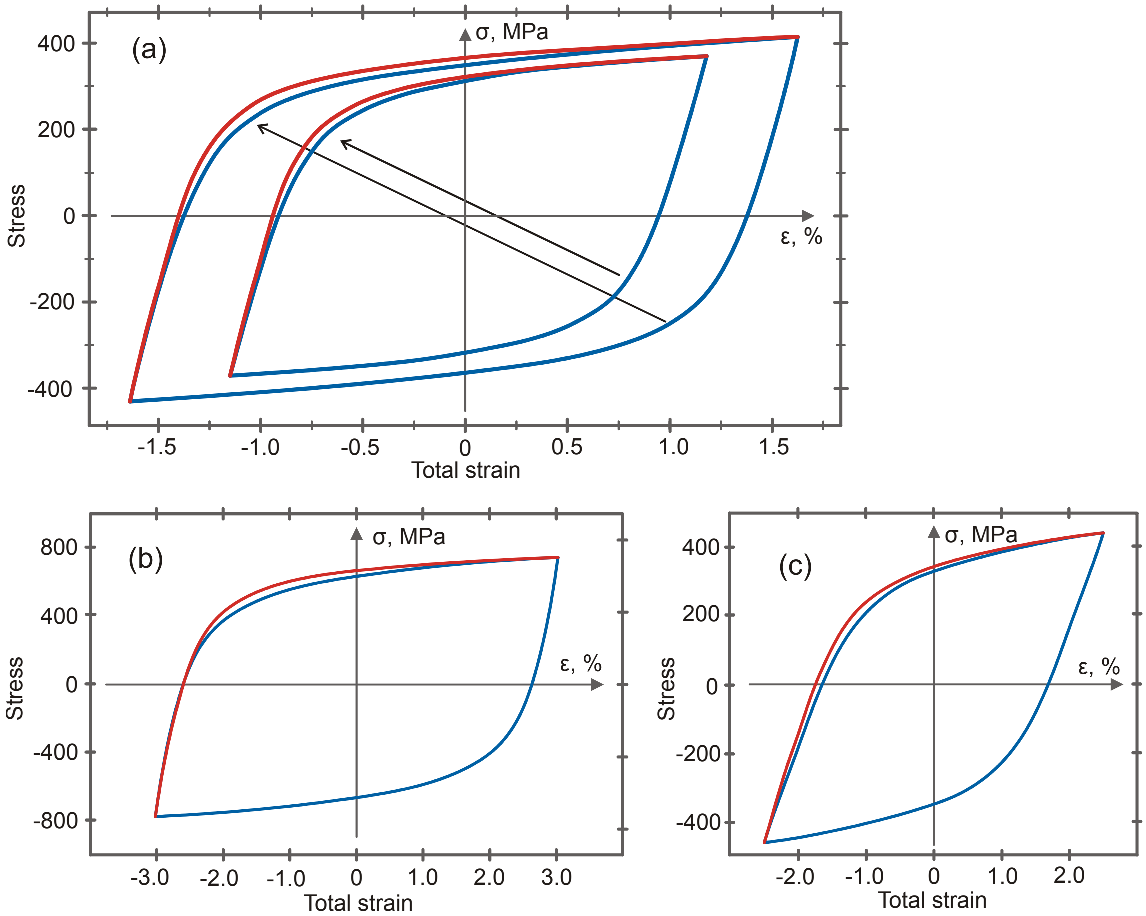

Fig. 22 – Difference between tensile and compression stress-strain curves for branches of stabilized hysteresis loops for (a) investigated S355J2 steel, (b) 304 stainless steel (experimental data from Kang et al. (2003)) and (c) 2124-T851 aluminum alloy (experimental data from Halama et al. (2017))

Equation (79) allows the isotropic hardening to develop differently in tensile and compression dominated loads, such that compression accelerates increasing of the size of the yield surface. However, for the low carbon steel S355 investigated in this study, it is established experimentally that elastic domain does not change during plastic strain accumulation in both tensile and compressive loading. Therefore, the influence of the first stress invariant should be inserted into the kinematic hardening rule. A new parameter D is then introduced only into the equation of kinematic hardening rule:

$$\dot{X}_{ij} = ABCD\exp\left(-\frac{2}{3}\frac{\left(X_{kl}-O_{kl}\right)n_{kl}}{B}\right)\dot{\varepsilon}^{p}_{ij} \tag{80}$$

The role of the parameter D is to provide variation of the slope of stress-strain curves whether tensile or compression stress state dominates. Based on the experimental observations, the evolution equation for the parameter is written in the form:

$$\dot{D} = d_1 d_2 \exp\left(-d_2\left|I_1\right|\right)\dot{I}_1 \tag{81}$$

or in terms of accumulated plastic strain rate:

$$\dot{D} = d_1 d_2 J \exp\left(-d_2\left|I_1\right|\right)\dot{p} \tag{82}$$

where d_1 and d_2 are material parameters and J is variation of the first stress invariant during accumulation of plastic strain:

$$J = \frac{\dot{I}_1}{\dot{p}} \tag{83}$$

Integration of the equation (82) for the uniaxial case with initial conditions of $D(0)=1$, yields:

$$D = d_1\left[1-\exp\left(d_2\sigma\right)\right]H\left(-\sigma\right) - d_1\left[1-\exp\left(-d_2\sigma\right)\right]H\left(\sigma\right) \tag{84}$$

The result of the integration is illustrated in Fig. 23. It is seen that tensile load lowers the parameter D below one, thereby leading for decrease in the stress-strain curve slope, whereas compressive load tends to increase the slope of the stress-strain curve. It is noted that in the case of pure shear loading conditions with $I_1 = 0$, the parameter D will not change and stay equal to one, meaning there is no additional change in the slope of deformation curves. Figure 24 shows application of the model to simulate stress-strain curves from upper and bottom branches of the hysteresis loop of S355J2 steel under strain amplitude of 1.6%. The stress-strain curves are plotted together with a point of zero stress at the origin. It is seen that the developed modelling approach for the first stress invariant conforms well to the experimental results. More examples with application of the developed model with a calibration procedure for finding material constants d_1 and d_2 are considered in the companion paper (Part II).

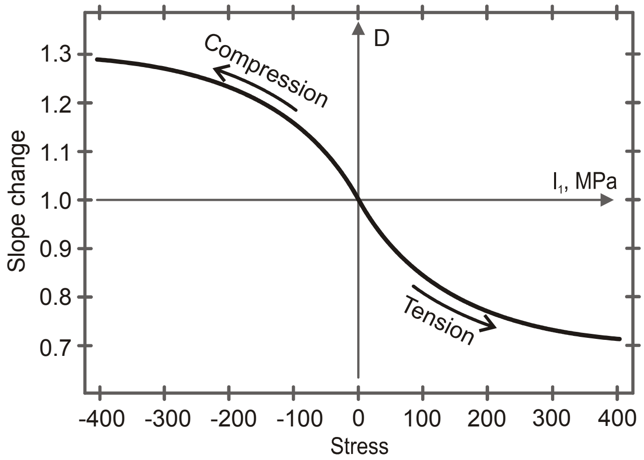

Fig. 23 – Evolution of parameter *D* with tensile and compression loading

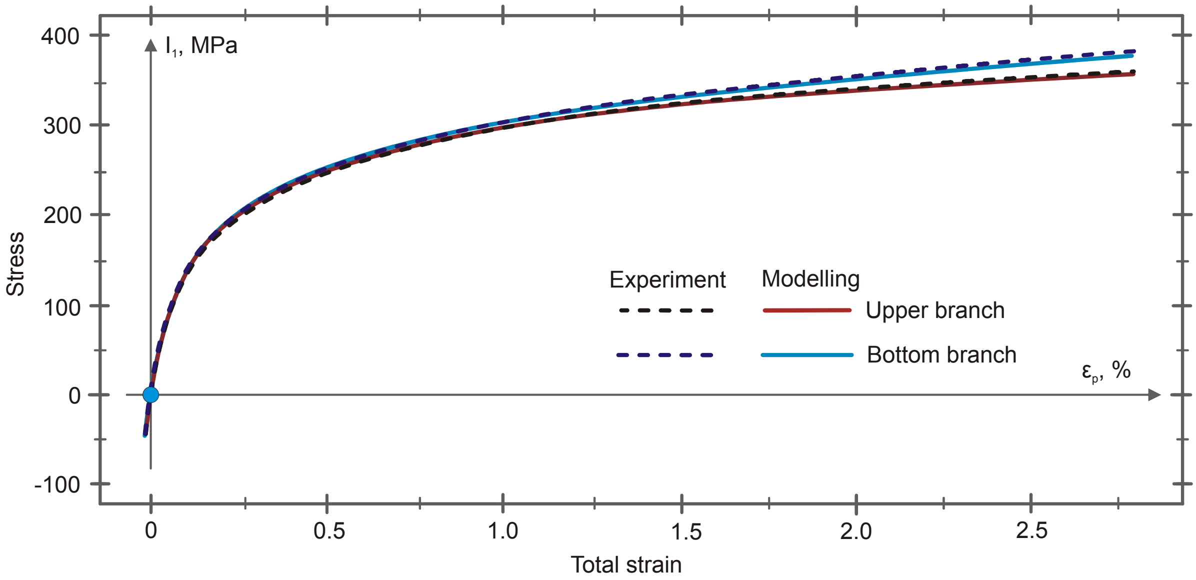

Fig. 24 – Upper and bottom branches of the hysteresis loop of S355J2 steel with modelling

It should be noted that in the models (Bai and Wierzbicki, 2008; Spitzig and Richmond, 1984) of the hydrostatic pressure effect, the first stress invariant is incorporated into the yield criterion without affecting kinematic or isotropic hardening functions. However, the experimental results from Voyiadjis et al. (2012) clearly showed that there is a difference for hardening in tension and compression dominated loading for DIN1.6959 steel. Therefore, the hydrostatic pressure effect should also be included into the hardening rules. As in this study no visible difference between measured yield stress during tension and compression was found, the effect of the first stress invariant is incorporated into the kinematic hardening rule only which determines the shape of the stress-strain curves.

14. Conclusions

This paper proposes a new continuum model of cyclic plasticity in metals, capable of accurate representation of complex cyclic stress-strain curves. The theoretical development is based on experimental results from cyclic tension-compression tests of S355J2 low carbon steel and experimental stress-strain curves from the literature. The review of the literature on phenomenological cyclic plasticity models with A-F kinematic hardening rules indicates certain restrictions in modelling cyclic plasticity responses with this approach. This is attributed to the number of back stress components, combined with evolution rule modifications, required to represent some aspects of the cyclic behaviour accurately. Here, a new approach based on an alternative kinematic hardening formulation is developed.

High accuracy of stress-stain curve shape description is achieved by introduction of a new kinematic hardening rule with a logarithmic function obtained after its integration. The model does not use back stress decomposition and the hardening slope of a stress-strain curve is modelled only with a few material parameters. Experimental studies showed that stress-strain curves from different loading stages share a similar form but differ in the way they occur in the deformation process. Therefore, a reference point for each stress-strain curve is introduced and all deformation process described by movement of this point. Two cases of the change of the reference point are determined from experimental observations for proportional loading. They are reversal of the loading path and returning to the previous loading path after loading reversal. To define an evolution rule for the reference point, a new framework of Dirac delta functions is developed. This can simulate stepwise dependence for the reference point as well as other internal variables discussed in a companion paper (Part II). The method for moving the reference point for uniaxial loading is generalized to multiaxial stress by introducing a reference back stress tensor and a supersurface with a linked subsurface, which are located outside the yield surface and define the evolution rule for the reference back stress tensor. The case of loading at the yielding plateau is incorporated by introduction of a new variable associated with the kinematic hardening rule that determines evolution of the subsurface. The developed approach has shown to be accurate in prediction of both the shape of the stress-strain curves and transition between curves at load reversals.

Differences between tensile and compression stress-strain curves are attributed to the influence of the first stress invariant. Its effect is incorporated into the kinematic hardening rule by an incremental form of dependency of the hardening slope on the first stress invariant. This approach is able to precisely adjust the stress-strain curve slope, whether tensile or compression stress state dominates, as well as include the cumulative nature of the first stress invariant dependence. The new form of kinematic hardening rule gives a high value of hardening at the reversal of load. This provides a smooth transition between elastic and elastic-plastic deformation. This allows cyclic plasticity modelling with accurate determination of the yield point (defined by a small offset value), such that elastic to elastic-plastic transition is modelled at the actual yield point of material. The ability of the model to simulate initiation of plasticity at the point of actual yield stress means that the nonlinearity of an unloading curve is included and the model naturally accounts for variation of unloading modulus during plastic strain accumulation without introduction of additional models to include this phenomenon.

The proposed modelling approach incorporates accurate isotropic hardening determination, improved description of the stress-strain curve, transition between curves during cyclic condition at loading reversals, variation of Young's modulus after plastic pre-straining and the effect of the first stress invariant in one mathematic model. To complete the model, additional experimental investigation and mathematical modelling of cyclic hardening/softening and ratcheting are considered in a companion paper (Part II), in which the model is validated experimentally.

Acknowledgments

This project has received funding from the European Union's Horizon 2020 research and innovation programme under the Marie Sklodowska-Currie grant agreement No 643159.

References

Abdel-Karim, M., 2011. Effect of elastic modulus variation during plastic deformation on uniaxial and multiaxial ratchetting simulations. European Journal of Mechanics - A/Solids. 30, 11-21.

Armstrong, P.J., Frederick, C., 1966. A mathematical representation of the multiaxial Bauschinger effect. Central Electricity Generating Board [and] Berkeley Nuclear Laboratories, Research & Development Department Berkeley.

Bai, Y., Wierzbicki, T., 2008. A new model of metal plasticity and fracture with pressure and Lode dependence. International Journal of Plasticity. 24, 1071-1096.

Ballarin, V., Perlade, A., Lemoine, X., Bouaziz, O., Forest, S., 2009. Mechanisms and Modeling of Bake-Hardening Steels: Part II. Complex Loading Paths. Metallurgical and Materials Transactions A. 40, 1375-1382.

Brünig, M., Berger, S., Obrecht, H., 2000. Numerical simulation of the localization behavior of hydrostatic-stress-sensitive metals. International Journal of Mechanical Sciences. 42, 2147-2166.

Brünig, M., Chyra, O., Albrecht, D., Driemeier, L., Alves, M., 2008. A ductile damage criterion at various stress triaxialities. International Journal of Plasticity. 24, 1731-1755.

Brünig, M., Gerke, S., 2011. Simulation of damage evolution in ductile metals undergoing dynamic loading conditions. International Journal of Plasticity. 27, 1598-1617.

BSI, 2000. BS EN 10250-2:2000. Open steel die forgings for general engineering purposes. Non-alloy quality and special steels. BSI.

Cazacu, O., Barlat, F., 2004. A criterion for description of anisotropy and yield differential effects in pressure-insensitive metals. International Journal of Plasticity. 20, 2027-2045.

Chaboche, J.L., 1979. Modelization on the Strain Memory Effect on the Cyclic Hardening of 316 Stainless Steel. Trans. of the 5th Int. Conf. on SMiRT. 11.

Chen, Z., Bong, H.J., Li, D., Wagoner, R.H., 2016. The elastic–plastic transition of metals. International Journal of Plasticity. 83, 178-201.

Dafalias, Y.F., Popov, E.P., 1975. A model of nonlinearly hardening materials for complex loading. Acta Mechanica. 21, 173-192.

Döring, R., Hoffmeyer, J., Seeger, T., Vormwald, M., 2003. A plasticity model for calculating stress–strain sequences under multiaxial nonproportional cyclic loading. Computational Materials Science. 28, 587-596.

Eisenträger, J., Naumenko, K., Altenbach, H., 2018a. Calibration of a phase mixture model for hardening and softening regimes in tempered martensitic steel over wide stress and temperature ranges. The Journal of Strain Analysis for Engineering Design. 53, 156-177.

Eisenträger, J., Naumenko, K., Altenbach, H., 2018b. Numerical implementation of a phase mixture model for rate-dependent inelasticity of tempered martensitic steels. Acta Mechanica. 229, 3051-3068.

Elliot, R.A., Orowan, E., Udoguchi, T., Argon, A.S., 2004. Absence of yield points in iron on strain reversal after aging, and the Bauschinger overshoot. Mechanics of Materials. 36, 1143-1153.

Goto, Y., Wang, Q., Obata, M., 1998. FEM Analysis for Hysteretic Behavior of Thin-Walled Columns. Journal of Structural Engineering. 124, 1290-1301.

Halama, R., Markopoulos, A., Jančo, R., Bartecký, M., 2017. Implementation of MAKOC cyclic plasticity model with memory. Advances in Engineering Software. 113, 34-46.

Hallai, J.F., Kyriakides, S., 2013. Underlying material response for Lüders-like instabilities. International Journal of Plasticity. 47, 1-12.

Hill, R., 1950. The Mathematical theory of plasticity, by R. Hill. The Clarendon Press, Oxford.

Jiang, Y., 2001. An Experimental Study of Inhomogeneous Cyclic Plastic Deformation. Journal of Engineering Materials and Technology. 123, 274-280.

Jiang, Y., Sehitoglu, H., 1996. Modeling of Cyclic Ratchetting Plasticity, Part I: Development of Constitutive Relations. Journal of Applied Mechanics. 63, 720-725.

Kang, G., Ohno, N., Nebu, A., 2003. Constitutive modeling of strain range dependent cyclic hardening. International Journal of Plasticity. 19, 1801-1819.

Kowalewski, Z.L., Szymczak, T., Maciejewski, J., 2014. Material effects during monotonic-cyclic loading. International Journal of Solids and Structures. 51, 740-753.

Lai, Y., Liao, M., Hu, K., 2016. A constitutive model of frozen saline sandy soil based on energy dissipation theory. International Journal of Plasticity. 78, 84-113.

Lamba, H.S., Sidebottom, O.M., 1978. Cyclic Plasticity for Nonproportional Paths: Part 2—Comparison With Predictions of Three Incremental Plasticity Models. Journal of Engineering Materials and Technology. 100, 104-111.

Lee, E.-H., Stoughton, T.B., Yoon, J.W., 2017a. A new strategy to describe nonlinear elastic and asymmetric plastic behaviors with one yield surface. International Journal of Plasticity. 98, 217-238.

Lee, J.-Y., Lee, M.-G., Barlat, F., Bae, G., 2017b. Piecewise linear approximation of nonlinear unloading-reloading behaviors using a multi-surface approach. International Journal of Plasticity. 93, 112-136.

Lee, J., Lee, J.-Y., Barlat, F., Wagoner, R.H., Chung, K., Lee, M.-G., 2013. Extension of quasi-plastic–elastic approach to incorporate complex plastic flow behavior – application to springback of advanced high-strength steels. International Journal of Plasticity. 45, 140-159.

Luo, L., Ghosh, A.K., 2003. Elastic and Inelastic Recovery After Plastic Deformation of DQSK Steel Sheet. Journal of Engineering Materials and Technology. 125, 237-246.

Mazière, M., Luis, C., Marais, A., Forest, S., Gaspérini, M., 2017. Experimental and numerical analysis of the Lüders phenomenon in simple shear. International Journal of Solids and Structures. 106-107, 305-314.

Mendiguren, J., Cortés, F., Gómez, X., Galdos, L., 2015. Elastic behaviour characterisation of TRIP 700 steel by means of loading–unloading tests. Materials Science and Engineering: A. 634, 147-152.

Mirone, G., Corallo, D., 2010. A local viewpoint for evaluating the influence of stress triaxiality and Lode angle on ductile failure and hardening. International Journal of Plasticity. 26, 348-371.

Mróz, Z., 1967. On the description of anisotropic workhardening. Journal of the Mechanics and Physics of Solids. 15, 163-175.

Naumenko, K., Altenbach, H., Kutschke, A., 2011. A Combined Model for Hardening, Softening, and Damage Processes in Advanced Heat Resistant Steels at Elevated Temperature. International Journal of Damage Mechanics. 20, 578-597.

Naumenko, K., Gariboldi, E., 2014. A phase mixture model for anisotropic creep of forged Al–Cu–Mg–Si alloy. Materials Science and Engineering: A. 618, 368-376.

Prager, W., 1949. Recent Developments in the Mathematical Theory of Plasticity. Journal of Applied Physics. 20, 235-241.

Shen, C., Mamaghani, I.H.P., Mizuno, E., Usami, T., 1995. Cyclic Behavior of Structural Steels. II: Theory. Journal of Engineering Mechanics. 121, 1165-1172.

Shen, W.Q., Zhang, J., Shao, J.F., Kondo, D., 2017. Approximate macroscopic yield criteria for Drucker-Prager type solids with spheroidal voids. International Journal of Plasticity. 99, 221-247.

Smith, J., Liu, W.K., Cao, J., 2015. A general anisotropic yield criterion for pressure-dependent materials. International Journal of Plasticity. 75, 2-21.

Spitzig, W.A., Richmond, O., 1984. The effect of pressure on the flow stress of metals. Acta Metallurgica. 32, 457-463.

Sun, L., Wagoner, R.H., 2011. Complex unloading behavior: Nature of the deformation and its consistent constitutive representation. International Journal of Plasticity. 27, 1126-1144.

Sun, Y., Gao, Y., Zhu, Q., 2018. Fractional order plasticity modelling of state-dependent behaviour of granular soils without using plastic potential. International Journal of Plasticity. 102, 53-69.

Taleb, L., Cailletaud, G., 2010. An updated version of the multimechanism model for cyclic plasticity. International Journal of Plasticity. 26, 859-874.

Ucak, A., Tsopelas, P., 2011. Constitutive Model for Cyclic Response of Structural Steels with Yield Plateau. Journal of Structural Engineering. 137, 195-206.

Ucak, A., Tsopelas, P., 2012. Accurate modeling of the cyclic response of structural components constructed of steel with yield plateau. Engineering Structures. 35, 272-280.

Voyiadjis, G.Z., Hoseini, S.H., Farrahi, G.H., 2012. A Plasticity Model for Metals With Dependency on All the Stress Invariants. Journal of Engineering Materials and Technology. 135, 011002-011002-011013.

Wang, X.-g., Huang, M.-x., 2017. Temperature dependence of Lüders strain and its correlation with martensitic transformation in a medium Mn transformation-induced plasticity steel. Journal of Iron and Steel Research, International. 24, 1073-1077.

Wang, Y.-B., Li, G.-Q., Cui, W., Chen, S.-W., Sun, F.-F., 2015. Experimental investigation and modeling of cyclic behavior of high strength steel. Journal of Constructional Steel Research. 104, 37-48.

Wilson, C.D., 2001. A Critical Reexamination of Classical Metal Plasticity. Journal of Applied Mechanics. 69, 63-68.

Xu, L., Nie, X., Fan, J., Tao, M., Ding, R., 2016. Cyclic hardening and softening behavior of the low yield point steel BLY160: Experimental response and constitutive modeling. International Journal of Plasticity. 78, 44-63.

Yang, M., Akiyama, Y., Sasaki, T., 2004. Evaluation of change in material properties due to plastic deformation. Journal of Materials Processing Technology. 151, 232-236.

Yoshida, F., Kaneda, Y., Yamamoto, S., 2008. A plasticity model describing yield-point phenomena of steels and its application to FE simulation of temper rolling. International Journal of Plasticity. 24, 1792-1818.

Yoshida, F., Uemori, T., Fujiwara, K., 2002. Elastic–plastic behavior of steel sheets under in-plane cyclic tension–compression at large strain. International Journal of Plasticity. 18, 633-659.

Yu, H.Y., 2009. Variation of elastic modulus during plastic deformation and its influence on springback. Materials & Design. 30, 846-850.

Zajkani, A., Hajbarati, H., 2017. Investigation of the variable elastic unloading modulus coupled with nonlinear kinematic hardening in springback measuring of advanced high-strength steel in U-shaped process. Journal of Manufacturing Processes. 25, 391-401.

Zang, S.L., Guo, C., Wei, G.J., Chen, F., Dong, W., Zhang, K., 2006. A new model to describe effect of plastic deformation on elastic modulus of aluminum alloy. Trans Nonferrous Met Soc China. 16, 1314-1318.

Zavattieri, P.D., Savic, V., Hector, L.G., Fekete, J.R., Tong, W., Xuan, Y., 2009. Spatio-temporal characteristics of the Portevin–Le Châtelier effect in austenitic steel with twinning induced plasticity. International Journal of Plasticity. 25, 2298-2330.

Zhang, J., Jiang, Y., 2005a. An experimental study of inhomogeneous cyclic plastic deformation of 1045 steel under multiaxial cyclic loading. International Journal of Plasticity. 21, 2174-2190.

Zhang, J., Jiang, Y., 2005b. Lüders bands propagation of 1045 steel under multiaxial stress state. International Journal of Plasticity. 21, 651-670.

Zhu, Y., Kang, G., Kan, Q., Bruhns, O.T., 2014. Logarithmic stress rate based constitutive model for cyclic loading in finite plasticity. International Journal of Plasticity. 54, 34-55.

Zhu, Y., Kang, G., Yu, C., 2017. A finite cyclic elasto-plastic constitutive model to improve the description of cyclic stress-strain hysteresis loops. International Journal of Plasticity. 95, 191-215.

Zhu, Y., Poh, L.H., 2016. A finite deformation elasto-plastic cyclic constitutive model for ratchetting of metallic materials. International Journal of Mechanical Sciences. 117, 265-274.